SURFACE ROUGHNESS FORMATION DURING TENSILE PLASTIC DEFORMATION OF NICKEL POLYCRYSTALS

by

KRANTHI BALUSU

Presented to the Faculty of the Graduate School of

The University of Texas at Arlington in Partial Fulfillment

of the Requirements

for the Degree of

DOCTOR OF PHILOSOPHY

THE UNIVERSITY OF TEXAS AT ARLINGTON

December 2018

`

Acknowledgments

I would like to sincerely thank Dr. Haiying Huang for the patience and foresight to guide me through long periods of demanding research. I would also like to thank her for pushing me to reach the high standards expected in academic research. I would also like to acknowledge the help Dr. Efstathios Meletis and Randall Kelton for their assistance in dealing with material science issues of the project, which were completely new to me. I also thank my dissertation committee for their guidance and valuable inputs without which this research would not have been completed. I am also grateful for the courses they have offered. These courses have helped me understand and model the mechanical behavior of solids.

I am grateful to the nation of the USA for providing an environment that is deeply conducive to productive academic research. Particularly, I acknowledge the Air Force Office of Scientific Research (AFOSR) grant that has helped me fund the majority of my research.

I am grateful to my colleagues and the friends I have made during this endeavor. Personal talks with them were as important as the technical discussions. I am especially grateful to Abhay Singh and Franck Tchafa, whose empathy and support has helped me push through the difficult periods of my research.

Finally, I would like to thank my family for their support of my aspirations. Particularly, I would thank my uncle Dr. Rao Balusu, whose practical advice has pushed me to bring my research to a timely conclusion. I am most thankful to my parents Syamala and Narendra, to whom I attribute many of the characteristics that help succeed in academic research.

September 5, 2018

Abstract

SURFACE ROUGHNESS FORMATION DURING

TENSILE PLASTIC DEFORMATION OF

NICKEL POLYCRYSTALS

Kranthi Balusu, PhD

The University of Texas at Arlington, 2018

Supervising Professor: Haiying Huang

Understanding the formation of surface roughness could help better diagnose a metal component's health and could potentially help in making better microstructure design decisions. Both of these, in turn, contribute to the design of efficient structural components. In this work, the research objective is to understand the relationship between the surface microstructure (i.e., grain orientations) and the surface-height changes in nickel polycrystals undergoing small amounts of tensile plastic deformation. The secondary objective is to determine the relationship between surface height and strain localization. Primarily simulations were used, along with experimental surface roughness observations, to validate the simulation results. Discrete dislocation plasticity (DDP) was used to simulate slip-step-type surface roughness, and the crystal plasticity finite element method (CPFEM) was used to simulate grain-scale surface roughness. Electron backscatter diffraction (EBSD) characterized the microstructure on the surface, and surface white light interferometer (SWLI) measured the surface heights of deformed samples. Randall Kelton, a Ph.D. candidate in Material science and Engineering, performed experiments and I focused primarily on simulations and analysis of experimental data.

The first phase of the work has an emphasis on simulating the surface roughness at the scale of the slip steps. Calculation of stress fields associated with dislocations at the surface is

essential in the simulation of slip-step formation. So, a novel, efficient way to simulate stress fields of dislocations at the free surface of 3D elastic, anisotropic materials was devised. Subsequently, it was found that DDP can only generate results at a much smaller scale than that of this study's experimental surface-height measurements.

In the second part of this work, the focus shifts to roughness at a greater length scale, the grain scale. First, the effect of grain orientation on its surface height was investigated, ignoring the role of the interaction of neighboring grains in roughness formation. Experimental and simulations have revealed that the plastic hardness of a grain does not determine the grain-surface height as previously thought. It was found that the plastic deformation of the grain's most stressed slip systems along the direction normal to the surface determines a grain's surface height. Simulations also indicated that plastic strains of a grain in the loading direction are not be related to its surface height. However, plastic strains in the other two directions can be potentially estimated using surface heights.

For many grain orientations, simulating the grain itself does not produce the experimentally observed surface behavior. The neighboring grains were found to be highly influential in determining a grain's surface height, especially the grains lying underneath the surface up to depths of 3–4 grain diameters. Thus, discrepancies between experiments and simulations are justified. While doing so, it was also found that a few specific grain orientations exhibit the same surface behavior irrespective of the neighboring grains.

The studies conducted in this research have led to an understanding of grain-scale surface roughness formation, and as a result, the limitations in predicting surface roughness using surface-grain orientations are that surface-height data can make only a limited diagnosis of strain localization.

Contents

List of illustrations

List of tables

Chapter 1

Introduction

Motivation

1. The efficient design of metal structural components requires the understanding and prediction of structural failure. Structural failure in ductile metals often follows localization events during plastic straining. Localization events such as crack initiation and necking can often be predicted by monitoring the roughness of the surfaces during plastic deformation [1]–[4]. This is a feasible approach because plastic deformation is the unified mechanism governing both surface roughening and failure. However, the exact relationship between strain localization and surface roughness is not well understood. Surface roughness results from out-of-plane plastic deformation and manifests itself due to the heterogeneity of the underlying microstructure in a polycrystalline metal. In this case, the relationship between the surface roughness formation and the underlying microstructure remains poorly understood.

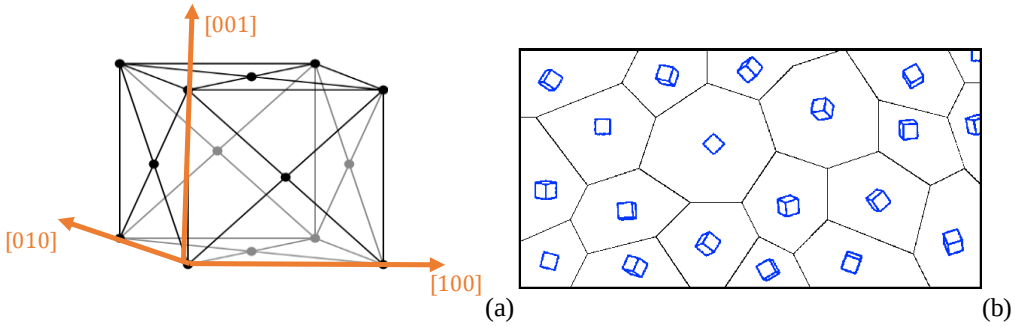

Figure 1-1. (a) FCC crystal lattice with the three axes representing the crystallographic coordinate system; (b) surface of a sample depicting orientations of the lattice in every grain.

The microstructure of the whole sample is expected to influence the sample's deformation behavior. However, using widely available techniques, only the surface microstructure can be characterized non-destructively. In pure, defect-free metal polycrystals, grains are the key microstructural features. Grains in a polycrystal are individual crystals with a unique lattice orientation. Figure 1-1(a) shows the lattice structure of nickel which is a face-centered crystal (FCC) lattice. Characterization using techniques such as electron backscatter diffraction (EBSD) allows us to determine the boundaries and orientation of each grain on the surface. The key research question is whether or not the microstructure information (i.e., grain orientation) from the surface can determine the surface roughness.

2. Objectives and approach

The primary of objective of this study is to understand the relationship between surface microstructure and surface roughness. The secondary objective is to determine the relationship between surface roughness features and strain distributions.

Our main approach to achieve the research objectives involves using simulations. The advantage of simulations lies in their ability to isolate individual features of the microstructure and vary these features while holding other parameters constant, thereby providing an in-depth understanding of the influence of the isolated feature on the results. While the slip of the atomic planes is the fundamental underlying plastic deformation mechanism, various modeling approaches are used to model microstructure sensitive deformation behavior at different scales, as shown in Figure 1-2[5]. The accuracy of the modeling approaches and their applicability to a particular scale of plastic deformation is still not well understood [6], [7]. That is why simulation methods supported by experimental observations are often used to study microstructure sensitive plastic deformation.

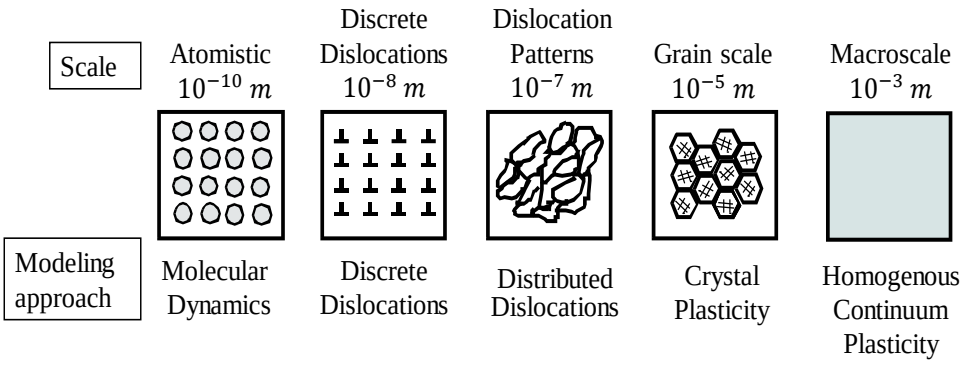

Figure 1-2. Length scales in the microstructure-sensitive modeling of materials.

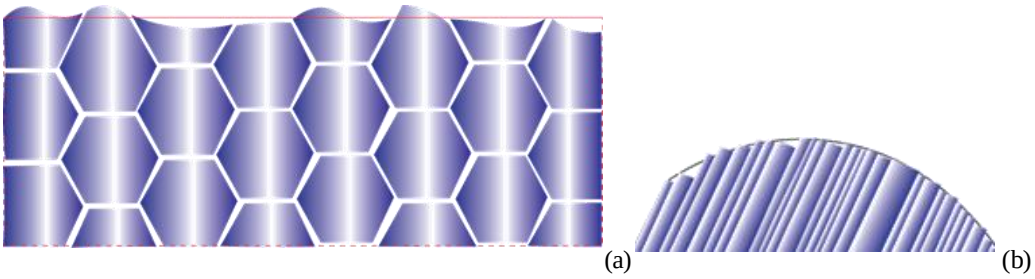

Figure 1-3. Profile of an initially smooth sample after plastic tensile deformation; (a) grain scale surface roughness; (b) inset from (a) illustrates slip steps.

Surface roughness in pure metals, such as nickel here, can be classified into two scales: grain scale (Figure 1-3 (a)) and slip steps (Figure 1-3(b)). Both these scales of surface roughness are considered in this study. Slip steps are features of the slip of atomic/lattice planes at the surface. However, it is not necessary to use atomic level simulations to model slip steps. Discrete dislocation lines, which separate the unslipped and slipped regions, can be used instead. Dislocation intersection with the surface is the origin of slip step formation. Plastic deformation consists of the movement,

multiplication, and interaction of these dislocations. Dislocations, depending on the lattice structure, have a specific magnitude and direction and move in specific lattice planes, making dislocation plasticity dependent on the microstructure. This modeling framework is called discrete dislocation plasticity (DDP), and it is suitable to simulate slip-step formation on the surface.

The unique plastic deformation of individual crystals toward the free surface leads to grain-scale surface roughness formation. The crystal plasticity finite element method (CPFEM) refers to models of crystal plasticity in a numerical implementation using finite elements. Crystal plasticity, at its most complex, uses the collective deformation mechanics of dislocations informed by simulations at lower scales, and the simplest approach uses phenomenological models [8]. All the approaches ignore modeling individual dislocations but still capture the unique deformation behavior of individual grains [6], [9]. Grain-scale roughness is intended to be simulated using phenomenological crystal plasticity models in CPFEM.

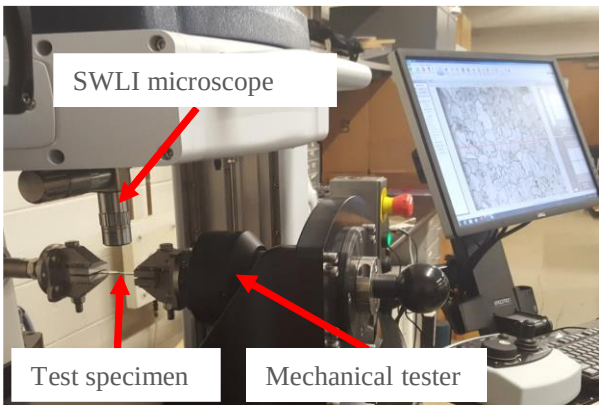

Figure 1-4. A scanning whitelight interferometer (SWLI) integrated with a mechanical tester for in-situ 3D surface profiling of the sample surface.

The microstructure on the surface of the gauge is characterized using electron backscatter diffraction (EBSD, Hitachi S-3000N SEM). We used a scanning white light Interferometer (SWLI,

Bruker NPFLEX) installed along with a tensile testing machine (Bose LM2 test bench) to record the surface heights in situ (see Figure 1-4). The SWLI surface profiler has a lateral resolution of 366 nm and a vertical resolution of less than 1 nm.

Dissertation organization

3. This dissertation is article based and consists of two manuscripts arranged as Chapters 2 and 3, which contain an extensive literature review on the simulation of slip-step and grain-scale roughness formation, respectively. Chapters 4 is dedicated to some preliminary work that is yet to be published. The first problem encountered is modeling slip-step formation. The current numerical approaches cannot effectively simulate elastic deformation near free surfaces. As a solution, the first paper, "A Combined Dislocation Fan–Finite Element (DF-FE) Method for Stress Field Simulation of Dislocations Emerging at the Free Surfaces of 3D Elastically Anisotropic Crystals," presents a novel, efficient numerical method. While this paper achieves its objectives, our experiments indicated that the surface roughness developed is dominated by the grain scale deformation instead of the slip band formation. Therefore, the focus shifted to simulate the grain-scale surface roughness.

In grain-scale surface roughness formation, we found that there is still a lack of a fundamental understanding of the relation between the grain orientation and grain-surface height. The relationship between grain orientation and its surface height is studied in the paper, "Investigating the Relationship Between Grain Orientation and Surface-Height Changes in Nickel Polycrystals Under Tensile Plastic Deformation", using both experimental and simulation approaches. We found that Schmid and Taylor factors, which depend only on the grain orientation in the loading direction, do not determine grain-surface height. We further discovered that, for most grains with a specific loading direction orientation, the orientation in the direction normal to the surface determines the grain-surface height. While the simulation results matched the experimental

observations for grains with the loading direction orientation near the [001] and [111] crystallographic directions. The simulated and measured surface behavior deviated for grains with other loading direction orientations. The dependence of these grains' surface behavior on the behavior of the grains around it could explain this phenomenon.

The first section of Chapter 4 contains a discussion of the second objective—determining the grain stresses and strains from a grain's surface height. For this purpose, the same simulation sample as the one presented in the previous chapter is used. We found that the strain and stress in the loading direction is dependent on the orientation in the loading direction but not related to grain-surface height. However, average grain surface heights are linearly related to stresses and strains in the normal and transverse directions. The second section investigates the role of neighboring grains in a grain's surface height. The results indicate that neighboring grains, especially grains directly underneath, have a substantial effect on surface height. As a consequence, for most orientations, the neighboring grains could determine a grain's surface behavior.

Chapter 2

A COMBINED DISLOCATION FAN – FINITE ELEMENT (DF-FE) METHOD FOR STRESS FIELD SIMULATION OF DISLOCATIONS EMERGING AT THE FREE SURFACES OF 3D ELASTICALLY ANISOTROPIC CRYSTALS

Kranthi Balusu, Haiying Huang

Balusu, K. & Huang, H., 2017. A combined dislocation fan-finite element (DF-FE) method for stress field simulation of dislocations emerging at the free surfaces of 3D elastically anisotropic crystals. Modelling and Simulation in Materials Science and Engineering, 25(3), p.0355007 (14pp).[1]

Abstract

A combined dislocation fan-finite element (DF-FE) method is presented for efficient and accurate simulation of dislocation nodal forces in 3D elastically anisotropic crystals with dislocations intersecting the free surfaces. The finite domain problem is decomposed into half-spaces with singular traction stresses, an infinite domain, and a finite domain with non-singular traction stresses. As such, the singular and non-singular parts of the traction stresses are addressed separately; the Dislocation Fan (DF) method is introduced to balance the singular traction stresses in the half-spaces while the Finite Element Method (FEM) is employed to enforce the non-singular boundary conditions. The accuracy and efficiency of the DF method is demonstrated using a simple isotropic test case, by comparing it with the analytical solution as well as the FEM solution. The DF-FE method is subsequently used for calculating the dislocation nodal forces in a finite elastically anisotropic crystal, which produces dislocation nodal forces that converge rapidly with increasing mesh resolutions. In comparison, the FEM solution fails to converge, especially for nodes closer to the surfaces.

Keywords: Dislocation fan - finite element method; Discrete dislocation dynamics; free surfaces; anisotropic elasticity; Stress field simulation; Peach-Koehler forces

1. Introduction

Understanding material plasticity is necessary for the optimal design of structures undergoing plastic deformation and fatigue. Plasticity, i.e., the permanent deformation of materials under static or cyclic loading, is generally attributed to internal dislocation activities. Persistent slip band (PSB) formation on the surfaces has long known to be a manifestation of material plastic deformation. In order to form the PSBs, the internal dislocation lines have to emerge and intersect the free surface. In other words, free surface– dislocation intersection is a crucial part of the slip band formation and nucleation mechanisms [10]. In addition, size effects [11] on the strength of

both single crystals [12] and polycrystals [13] are affected by free surface interaction. Free surface interaction is also required to explain the size effect on hardness in nanoindentation [14].

In recent years, discrete dislocation dynamics (DDD) simulation has made great advances in simulating plasticity at a microscopic scale, due to ever-increasing computation capabilities [15], [16]. In DDD simulations, dislocation is modeled as a line defect in a linear elastic body. A set of kinematic equations, typically obtained through molecular dynamics simulation, are used to govern the motion of individual dislocation in terms of the net forces acting on the dislocation due to external loading, defects, and other dislocations. The determination of dislocation stress fields and the corresponding dislocation nodal forces, therefore, is the most fundamental solution of any DDD simulation model. While the stress field solution for dislocation structures in an infinite domain is analytical [17], [18], the analytical stress field expressions for finite domains, however, are only available for a few specific domain shapes [19]–[24] and are also sometimes complicated to evaluate [25]. A common approach for finding the dislocation stress field in a generically shaped domain involves generating an image stress field to correct the stress field of the dislocations in infinite bodies and enforce the required boundary conditions [26]. For generalized domain shapes, numerical methods are often necessary to generate these image stress fields. Various methods, including the Finite Element Method (FEM) [27]–[30], Boundary Element Method [31], point force distribution [32], and surface dislocation loops [33] etc. have been developed in the past to obtain the dislocation stress field solution in finite bodies.

The aforementioned numerical simulation methods, however, cannot efficiently simulate the stress field of dislocation structures intersecting a free surface, due to the stress singularity at the intersecting point. Balancing these singular stresses requires a high mesh resolution at locations close to the intersection point [32], [34]. In a DDD simulation, this adaptive meshing has to be carried out at every time step and for a large number of intersecting dislocations. Since this would incur impractical computational burdens, adaptive meshing has not been used in full-scale DDD

simulations. Rather, a uniform mesh is usually used, and the solution converges only for meshes as fine as the lattice spacing [35], which is also impractical.

To address the singularity issue introduced by a dislocation intersecting with the surface of an isotropic body, Tang et al. presented a hybrid method, in which the image stress is a superposition of analytical and FEM solutions [36]. The closed-form solution of a semi-infinite dislocation line intersecting the free surface of the isotropic half-space [22] was used to remove the singular tractions that need to be corrected. The remaining non-singular surface stresses were balanced by the image stresses solution calculated from FEM. This hybrid method has been shown to be more accurate and efficient than using FEM alone. However, it is only applicable to isotropic materials. Although most researchers have used isotropic models in DDD, almost all metallic crystals are elastically anisotropic, making it natural to consider elastic anisotropy [37]–[39]. Considering anisotropic elasticity in DDD is particularly necessary for some crystals that are strongly anisotropic. For example, in highly anisotropic α-Fe, Frank-Read activation stresses [40] and dislocation pile-ups [41], aspects that strongly influence the plastic behavior, are significantly different when anisotropy is considered. Moreover, experimentally observed sharp corners in dislocation loops can only be simulated when anisotropy is considered [42]. Unfortunately, simulating anisotropic elasticity incurs additional computational effort in already expensive DDD simulations. Evaluating the stress fields of dislocation structures in infinite elastically anisotropic domains itself involves greater computational expense [43] because they either requires evaluation of an Eigenvalue problem or numerical integration [18]. Therefore, the method to balance the traction stress along the surfaces of a finite domain has to be as efficient as possible in order to keep the computational burden manageable.

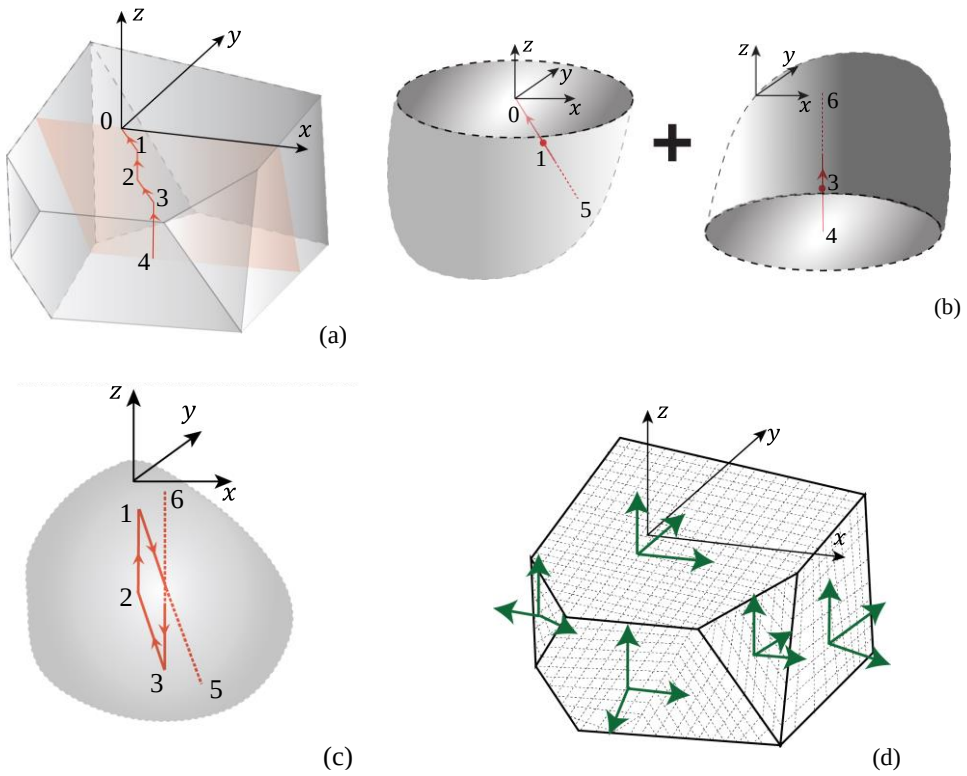

Figure 2-1. The decomposition process involved in the combined DF-FE method; *(a)* a dislocation intersecting the free surfaces at top and bottom surfaces of a representative finite domain; *(b)* semi –infinite dislocations (0-1-5) and (4-3-6) intersecting the free surfaces of the half-spaces; *(c)* the original dislocation structure, with the segments (0-1) and (4-3) removed and replaced by corresponding coincident lines extending to infinity away from the free surface. These lines start at nodes 1 and 3 and are in the opposite directions to the original. Note that the summation of the dislocation structures in *(b)* and *(c)* is equivalent to the original dislocation structure in *(a); (d)* the body meshed as finite elements to enforce the stress boundary conditions. The image tractions are shown in green.

In this work, we present a combined dislocation fan – finite element (DF-FE) method to simulate the stress field of a dislocation intersecting the free surfaces of a finite anisotropic body,

extending the approach presented in Tang et al. (2006) from isotropic to anisotropic elasticity. Dislocation fan (DF) has been previously developed for analyzing the elastic energy and image forces on the semi-infinite intersecting dislocation in elastically anisotropic half-spaces [44]. In this paper, we developed a numerical implementation of the DFs to remove the singular stresses of dislocation lines emerging at the surfaces of elastically anisotropic spaces. As such, the finite element model is only needed to enforce the non-singular traction-force and displacement boundary conditions. Since the singularity is addressed by the DFs instead of the FEs, adaptive meshing in the FE model is no longer necessary. A uniform mesh is sufficient to account for dislocation motions. More importantly, the FE model can still converge with a coarse mesh, increasing the efficiency of the DDD simulation significantly.

2. Methodology

The problem that we intend to solve is the stress field of an arbitrary dislocation structure in a finite body that has dislocations intersecting its free surfaces, as shown in Figure 2-1(a). This finite body can be of any shape to represent a single crystal or even a grain in polycrystalline materials. The surfaces that the dislocation intersects can be of any arbitrary orientation. For illustration purposes, however, we assume the dislocation structure intersects the top and bottom surfaces of the finite body. In case the surfaces the dislocation intersects are curved, the surface near the point of intersection can be approximated as being locally flat. For computational purposes, the dislocation structure is discretized into straight segments denoted by nodal numbers. The stress field of such a dislocation structure, at an arbitrary point $\boldsymbol{x}$ in the finite body, can be decomposed into individual stress contributions as

$$\boldsymbol{\sigma}(\boldsymbol{x}) = \boldsymbol{\sigma}^{\mathrm{hsI}}(\boldsymbol{x}) + \boldsymbol{\sigma}^{\mathrm{hsII}}(\boldsymbol{x}) + \boldsymbol{\sigma}^{\mathrm{inf}}(\boldsymbol{x}) + \boldsymbol{\sigma}^{\mathrm{img}}(\boldsymbol{x}), \tag{2.1}$$

where $\boldsymbol{\sigma}^{\mathrm{hsI}}(\boldsymbol{x})$ and $\boldsymbol{\sigma}^{\mathrm{hsII}}(\boldsymbol{x})$ are the stress fields of the two semi-infinite dislocations in half-spaces as shown in Figure 2-1(b). $\boldsymbol{\sigma}^{\mathrm{inf}}(\boldsymbol{x})$ is the stress field of the dislocation component in an

infinite elastically anisotropic medium shown in Figure 2-1(c). $\boldsymbol{\sigma}^{\text{img}}(\boldsymbol{x})$ is the correction image stress for the remaining traction stresses along the boundaries (see Figure 2-1(d)). It is worth noting that $\boldsymbol{\sigma}^{\text{img}}(\boldsymbol{x})$ does not have any singular traction stresses. As such, it can be solved using conventional stress-analysis methods, such as FEM, BEM, etc.

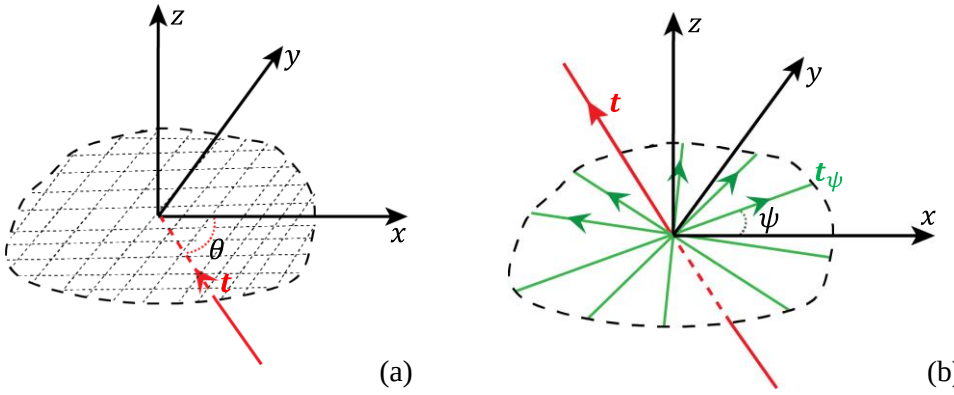

Figure 2-2. *(a)* A semi-infinite dislocation line emerging on the free surface (z=0) of an elastically anisotropic half-space. The dislocation line is defined by the vector $\boldsymbol{t}$. It lies in the zx-plane and makes an angle θ with the x axis; *(b)* the same problem as a superposition of an infinite

For traction-free surfaces, the boundary conditions can be expressed as

$$\boldsymbol{\sigma}(\boldsymbol{x}) \cdot \boldsymbol{n}^0 = 0, \tag{2.2}$$

where $\boldsymbol{\sigma}(\boldsymbol{x})$ is the stress tensor at point $\boldsymbol{x}$ on the free surfaces and $\boldsymbol{n}^0$ is the vector normal to the free surfaces. The dot in equation (2.2) represents a convolution by one index. The combined DF-FE approach doesn't pose any extra limitations on the boundary conditions that can be enforced on any of the surfaces. Instead of a traction-free condition in equation (2.2), a finite traction boundary condition can be enforced by the addition of the required traction to the stress boundary conditions in FEM. Zero displacement boundary conditions are often used to model impenetrable grain boundaries in polycrystals [13], [45]. FEM alone can be used to set any required displacement boundary conditions on a surface with or without a dislocation intersection, since its displacement

field has no singularities. Similarly, surfaces with no intersecting dislocations, i.e. no singular stress fields, requires no special treatment and thus their boundary conditions can be set through the usual superposition approach using FEM.

Among the four stress components given in equation (2.1), the analytical solution for $\boldsymbol{\sigma}^{\mathrm{inf}}(\boldsymbol{x})$ is well-known [18] and $\boldsymbol{\sigma}^{\mathrm{img}}(\boldsymbol{x})$ can be obtained using conventional FEM. The stress field of a semi-infinite dislocation line intersecting the free surface of an elastically anisotropic half-space, i.e. $\boldsymbol{\sigma}^{\mathrm{hsI}}(\boldsymbol{x})$ and $\boldsymbol{\sigma}^{\mathrm{hsII}}(\boldsymbol{x})$, is given by the discretized Dislocation Fan (DF) method. In DF method, the stress field of a semi-infinite dislocation line intersecting the surface of a half-space, as shown in Figure 2-2(a), is equivalent to the stress field of an infinite body containing an infinite dislocation line and a dislocation fan on the z=0 plane, as defined in Figure 2-2(b). The dislocation fan is introduced to generate image stresses to cancel out the stresses of the dislocation line on the z=0 surface. The superposition of these two stresses fields thus satisfied the traction-free boundary condition of the half-space. A dislocation fan consists of a continuous distribution of virtual infinite dislocation lines on the surface centered on the intersection point between the free surface and the infinite dislocation. Each infinite dislocation line in the fan is defined by an angle ψ with respect to the x-axis. The solution for finding the Burgers vector of each dislocation in the fan, originally derived by Lothe et al. (1982) [44], is re-arranged in a more logical way and is summarized in the appendix. Once the Burgers vector of the dislocation fan $\boldsymbol{b}(\psi)$ is known, the stresses at any generic point due to the dislocation fan can be obtained numerically by discretizing the fan into individual dislocations at specific locations ψ_i, i.e.

$$\boldsymbol{b}(\psi_i) = \boldsymbol{b}(\psi)\,\Delta\psi_{i,i+1}\,, \tag{2.3}$$

where $\Delta\psi_{i,i+1}$ is the angular spacing between the adjacent dislocations at locations ψ_i and ψ_{i+1}. The stress field in an elastically anisotropic half-space is then a summation of the stress fields of each of these individual dislocation lines in the fan [17] and the intersecting dislocation.

3. Results and Discussions

3.1. Stress field of a dislocation intersecting the surface of an isotropic half-space

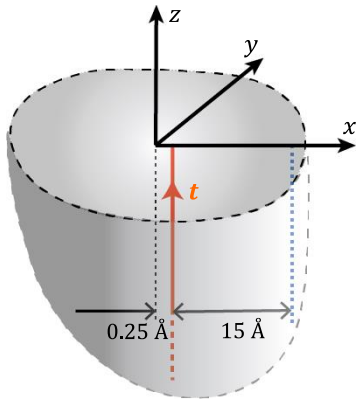

Figure 2-3. The test case for validating the discretized Dislocation Fan Method. The semi-infinite dislocation line is shown in red and is represented by the vector ***t***. It intersects the free surface (z = 0) of the half-space at an normal angle. The sampling line is shown in blue; it lies in the zx-plane and is parallel to the dislocation.

The accuracy of the DF method was validated first by comparing it with the analytical solution in an isotropic half-space, i.e. the Eshelby twist formalism for a semi-infinite screw dislocation line intersecting the free surface at a normal angle [46] (see Figure 2-3). The material is assumed to have a Young's modulus of $E = 200$ GPa and a Poisson's ratio of $\nu = 0.31$. The global coordinate system is set up assuming the z axis is normal to the free surface. A semi-infinite screw dislocation line, with a Burgers vector of magnitude $|\boldsymbol{b}| = 2.86$ Å, lies normal to the free surface. The stress field is sampled along a vertical line in the zx-plane that is parallel to the dislocation and separated by a distance of 15 Å from the dislocation line. Stress field simulation is most difficult to simulate closest to the point of intersection i.e. close to the unbalanced traction singularity. As

sampling distance increases, results from any numerical method would be clearly more accurate. The distance of 15 Å was chosen because linear elasticity is valid only beyond this distance.

To gauge the computational efficiency of the DF method, the problem defined in Figure 2-3 was also solved using a commercial FE simulation tool, ANSYS. The simulated domain is a cuboid of dimensions $30 \times 30 \times 12$ nm in x, y and z directions with the origin at the center of the topmost surface. The topmost surface is assumed to be traction free while the other five sides are assumed to be under zero displacement condition. These boundary conditions and the finite domain are good approximations for a half-space, especially for stress field simulation near the center of the domain and close to the free surface [35]. Uniform 8-node cuboid elements were used to mesh the finite domain and equal numbers of element divisions were chosen for each side of the domain. Since there is a node at the origin, the point at which the dislocation line intersects the topmost surface was set to be at $x = 0.25$ Å. In this work, the element size is denoted as the 'grid size', which is the largest length of the elements. The stresses at locations that are not coincident with the nodes were linearly interpolated from the nodal stress values averaged from adjacent elements. For grid sizes ranging from 15 Å (8000 elements) to 2.14 Å (2.7 million elements), the FE computational time ranged from 2 minutes to 24 hours in a workstation with an Intel core i7 processor and 28 GB RAM. In comparison, the numerical implementation of a dislocation fan with 180 equally spaced lines to calculate the stress field at 1000 points requires around two minutes and the computation time is linearly proportional to the sampling points.

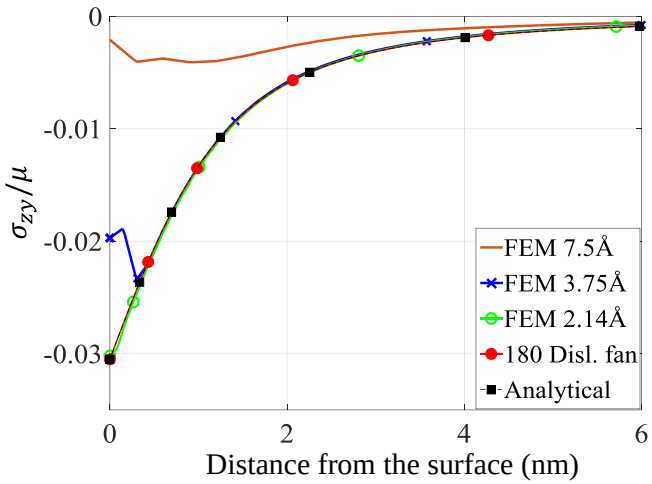

Figure 2-4. Comparison of results from the discretized Dislocation Fan Method, Finite Element Method, and analytical solution.

The DF method and FEM calculations of the image stress component σ_{zy} at different locations along the sampling line are compared with the analytical solution in Figure 2-4. The stress values are non-dimensionalized by normalizing them with the shear modulus μ. Two dislocation fans, one with 180 dislocations and the other with 360 dislocations were evaluated, which produced maximal deviations of 0.001% and 0.002% from the analytical solution, respectively. Since the improvement upon increasing the fan resolution is insignificant, only the results from the 180 discrete dislocations fan are presented. The FEM results of comparable accuracy requires meshes at the sizes of lattice dimensions, which took hours of computational time in contrast to a few minutes required for a DF method simulation.

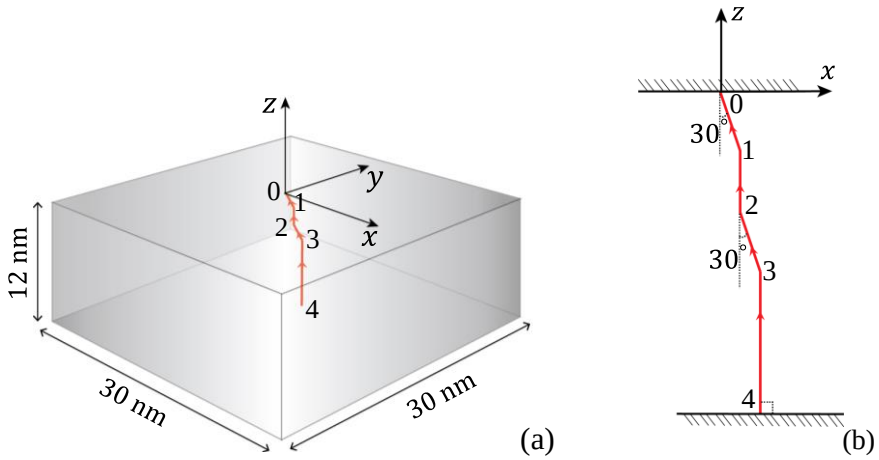

Figure 2-5. (a) A finite crystal with a dislocation structure intersecting the top and bottom free surfaces; (b) Orientation of the dislocation structure in the zx-plane. It consists of three 2 nm long dislocation segments and segment (3-4) extends to intersect the bottom free surface normally.

3.2. Dislocation nodal forces in a finite elastically anisotropic crystal

The test case for calculating the dislocation nodal forces in a finite elastically anisotropic crystal is depicted in Figure 2-5. The dislocation structure consists of four line segments with the ends intersecting the top and bottom surfaces of the cuboid (see Figure 2-5(a)). Surfaces at the left and the right are also assumed to be traction-free, while surfaces on the front and the back are set with zero displacement conditions. The segments are assumed to lie in the zx-plane and their orientations are shown in Figure 2-5(b). The simulated domain is a cuboid of dimensions $30 \times 30 \times 12$ nm in x, y and z directions with the origin at the center of the topmost surface. The material of the finite domain was assumed to be nickel with the elastic parameters of $C_{11} = 251.6$ GPa, $C_{12} = 154.4$ GPa, and $C_{44} = 122.0$ GPa [47]. The zx-plane represents the lattice slip plane (111) while

the z axis represents the Burgers vector $\frac{1}{2}[0\bar{1}1]$. The magnitude of the Burgers vector $|\boldsymbol{b}|$ is 2.86 Å. The FEM simulation was performed using the mesh specified in section 3.1.

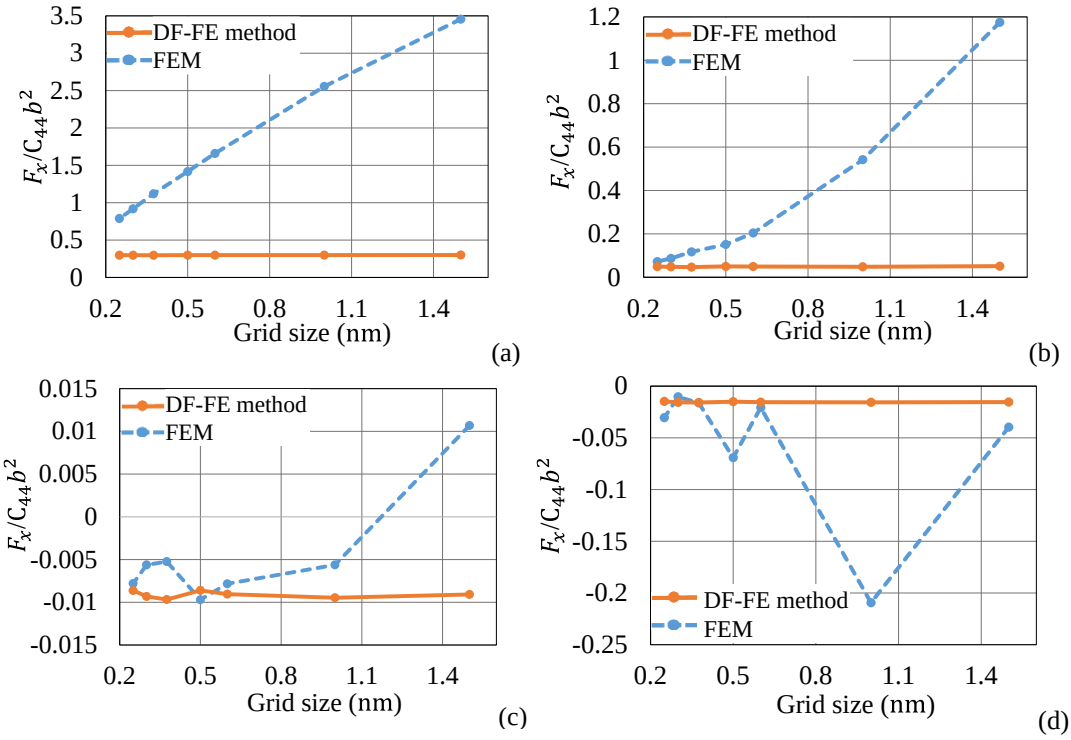

Figure 2-6. Simulated dislocation nodal forces in x direction. The forces are calculated using both the hybrid DF-FE method and FEM at multiple grid sizes. The forces are non-dimensionalized; *(a)* force on node 0, i.e. the node on the top free surface; *(b)*, *(c)* and *(d)* forces on nodes 1, 2 and 3 respectively; *(e)* force on node 4, i.e. the node on the free surface at the bottom.

Once the stress field is determined from equation (2.1), the force on the dislocation per unit length, i.e. the Peach-Koehler force $\boldsymbol{f}^{\mathrm{PK}}(\boldsymbol{x})$ at an arbitrary point $\boldsymbol{x}$ on the dislocation, can be calculated as

$$\boldsymbol{f}^{\mathrm{PK}}(\boldsymbol{x}) = (\boldsymbol{\sigma}(\boldsymbol{x}) \cdot \boldsymbol{b}) \times \boldsymbol{t}\,, \tag{2.4}$$

where the tensor $\boldsymbol{\sigma}(\boldsymbol{x})$ is the total stress field, $\boldsymbol{b}$ is the dislocation Burgers vector and $\boldsymbol{t}$ is the unit vector denoting the local dislocation orientation. Equation (2.4) is valid for any generalized dislocation structure. For a dislocation structure discretized as straight segments, the force on each segment is distributed among its dislocation nodes using a suitable linear weight function, $N_i(\boldsymbol{x})$. The force $\boldsymbol{F}_i^{(ij)}$ on node i from the segment with nodes at $\boldsymbol{x}_i$ and $\boldsymbol{x}_j$ can expressed as

$$\boldsymbol{F}_i^{(ij)} = \int_{\boldsymbol{x_i}}^{\boldsymbol{x_j}} N_i(\boldsymbol{x})\, \boldsymbol{f}^{\mathrm{PK}}(\boldsymbol{x}) dl(\boldsymbol{x}), \qquad \text{where } N_i(\boldsymbol{x}) = \frac{|\boldsymbol{x}-\boldsymbol{x}_j|}{|\boldsymbol{x}_j-\boldsymbol{x}_i|}\,. \tag{2.5}$$

The integral in equation (2.5) has to be evaluated numerically. To avoid stress singularities at locations close to a dislocation, an approximation scheme utilizing a dislocation core radius equal to the Burgers vector magnitude was used [43]. This method neglects all the stress contributions from the dislocation segments lying within a core radius around a stress sampling point.

Figure 2-6 shows the convergence of the nodal forces along the x direction with decreasing grid sizes. The hybrid DF-FE method produced results that converge rapidly. When the grid size was decreased from 1.5 nm to 0.25 nm, the maximum change of the nodal force contribution from the surfaces is only 3%. This indicates that the largest grid size used, i.e. 1,.5 nm, is sufficient for an accurate simulation of the nodal forces in this domain. In contrast, the FEM results don't converge for all five dislocation nodes, even at very small grid sizes. In particular, the results for nodes 3 and 4 show significant fluctuations. However, the FEM results do show a trend of convergence towards the hybrid DF-FE method results. At the grid size of 0.25 nm, the FEM results differ from the hybrid method's by 165%, 46.6%, 9.6%, -106% and -5120% at nodes 0, 1, 2, 3 and

4 respectively. Therefore, we can infer that the hybrid method can produce more accurate results than FEM, especially for the nodes on or close to the surface. Another observation is that when using the FEM, forces on a dislocation normally intersecting the free surface, e.g., segment (3-4), show worse convergence when compared to a dislocation that intersects the surface at an angle, e.g., segment (0-1).

4. Conclusion

This paper presents a combined DF-FE method to calculate stress fields of dislocations intersecting the free surfaces of elastically anisotropic crystals. The DF method is introduced to balance the singular tractions associated with a dislocation intersection, and FEM is used to balance the non-singular traction. Treating the singular and non-singular stresses using two different methods allows the solution to converge at a much coarser mesh and achieving excellent accuracy when compared to traditional methods. The presented work is intended to ease the computational burden in incorporating free surfaces and other boundary conditions in already expensive anisotropic DDD simulations. Combining this work with other recent developments [48]–[50] might make large-scale DDD simulations feasible. Another application of the presented hybrid method that we intend to pursue is the static simulation of surface stresses associated with persistent slip bands, which in turn might give insights into grain boundary penetration of slipbands (Hall-Petch effect) and crack initiation.

Appendix A. Stress field of a semi-infinite dislocation intersecting the free surface of an elastically anisotropic half-space

The stress field $\boldsymbol{\sigma}^{\mathrm{hs}}(\boldsymbol{x})$, at a point denoted by a vector $\boldsymbol{x}$ in the half-space, is decomposed as

$$\boldsymbol{\sigma}^{\mathrm{hs}}(\boldsymbol{x}) = \boldsymbol{\sigma}^{\mathrm{i}}(\boldsymbol{x}) + \boldsymbol{\sigma}^{\mathrm{f}}(\boldsymbol{x}), \tag{A.1}$$

Where $\boldsymbol{\sigma}^{\mathrm{i}}(\boldsymbol{x})$ and $\boldsymbol{\sigma}^{\mathrm{f}}(\boldsymbol{x})$ are the stress fields of the infinite dislocation line and the dislocation fan in the infinite body. The Burgers vector of the dislocation fan can be calculated by enforcing the traction free condition, i.e.

$$\boldsymbol{\sigma}^{\mathrm{hs}}(\boldsymbol{x}) \cdot \boldsymbol{n}^{0}|_{z=0} = 0, \tag{A.2}$$

where $\boldsymbol{n^0}$ is the normal to the surface. Combining equations (A.1) and (A.2) leads to

$$\boldsymbol{\sigma}^{\mathrm{f}}(\boldsymbol{x}) \cdot \boldsymbol{n}^{0}|_{z=0} = -\boldsymbol{\sigma}^{\mathrm{i}}(\boldsymbol{x}) \cdot \boldsymbol{n}^{0}|_{z=0} \tag{A.3}$$

The stress field of an infinite dislocation line in an infinite body, i.e. $\boldsymbol{\sigma}^{\mathrm{i}}(\boldsymbol{x})$, can be found using various formalisms [18]. Since the dislocation line has an infinite length, all points along a line that is parallel to the dislocation line have identical stress components. Therefore, the 3D infinite domain can be reduced to a 2D plane that is perpendicular to the dislocation line $\boldsymbol{t}$. Assume that xy-plane of the global xyz coordinate system is the horizontal plane and the dislocation line $\boldsymbol{t}$ falls in the xz-plane, for a point P_1 in the 3D space, an orthogonal local coordinate system $\{\boldsymbol{t}, \boldsymbol{m}, \boldsymbol{n}\}$ can be defined in such a way that the $\boldsymbol{mn}$-plane contains P_1 and the unit vector $\boldsymbol{n}$ is parallel to the y axis, as shown in Figure 2-7. Another orthogonal basis $\{\boldsymbol{m_\varphi}, \boldsymbol{n_\varphi}, \boldsymbol{t}\}$ can be defined by rotating $\boldsymbol{m}$ and $\boldsymbol{n}$ vectors an angle φ about $\boldsymbol{t}$. The stress field tensor at $P_1\ (\rho_1, \varphi_1)$ is then given as [51]

$$\begin{aligned}&\boldsymbol{\sigma}^{\mathrm{i}}(\rho_1, \varphi_1)\\ &= \frac{1}{2\pi^2\rho_1}\int_0^{\pi} d\varphi\ \frac{\left[\boldsymbol{C}\cdot\boldsymbol{m}_\varphi - (\boldsymbol{C}\cdot\boldsymbol{n}_\varphi)\left(\boldsymbol{n_\varphi n_\varphi}\right)^{-1}(\boldsymbol{n_\varphi m_\varphi})\right]\cdot\boldsymbol{b_0}}{\sin(\varphi-\varphi_1)},\end{aligned} \tag{A.4}$$

where $\boldsymbol{b}_0$ is the Burgers vector of the infinite dislocation line and $\boldsymbol{C} = C_{ijkl}\ \forall\, i,j,k,l = 1,2,3$ is the elastic stiffness tensor. Here, for any two real vectors $\boldsymbol{a}$ and $\boldsymbol{d}$, a designation is introduced such that

$$(\boldsymbol{ad})_{jk} = a_i C_{ijkl} d_l, \tag{A.5}$$

and $(\boldsymbol{ad})^{-1}$ is the inverse of the $(\boldsymbol{ad})$ matrix.

To calculate the traction forces generated by the dislocation fan, each infinitely long dislocation line $\boldsymbol{t}_\psi$ is assumed to have an infinitesimally small Burgers vector,

$$d\boldsymbol{b} = \boldsymbol{b}(\psi)\, d\psi. \tag{A.6}$$

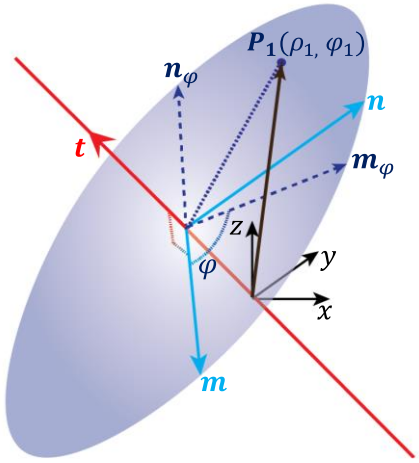

Figure 2-7. A point P_1 is denoted by the polar coordinates (ρ_1, φ_1) in the $\boldsymbol{mn}$-plane of the local orthogonal coordinate system $\{\boldsymbol{m}, \boldsymbol{n}, \boldsymbol{t}\}$. The unit vector $\boldsymbol{n}$ is defined to be parallel to the y axis. The orthogonal vectors $\boldsymbol{m}_\varphi$ and $\boldsymbol{n}_\varphi$ are obtained by rotating the $\boldsymbol{m}$ and $\boldsymbol{n}$ vectors by an angle φ about $\boldsymbol{t}$.

The traction stresses generated by this dislocation line at the point P_1 on the surface are [17]

$$\boldsymbol{n}^0 \cdot \boldsymbol{\sigma}^{\mathrm{t}\Psi}(r_1, \psi_1)|_{z=0} = \frac{\boldsymbol{B}(\psi) \cdot d\boldsymbol{b}}{2\pi d}, \tag{A.7}$$

where $d = r_1 \sin(\psi_1 - \psi)$ is the distance between the point P_1 and the dislocation line (see figure A2(b)). $\boldsymbol{B}(\psi)$ is known as the energy matrix and can be evaluated using Stroh formalism as shown below. A matrix $\boldsymbol{N}$ is defined as

$$\boldsymbol{N} = \begin{bmatrix} (\boldsymbol{nn})^{-1}(\boldsymbol{nm}) & (\boldsymbol{nn})^{-1} \\ (\boldsymbol{mn})(\boldsymbol{nn})^{-1}(\boldsymbol{nm}) - (\boldsymbol{mm}) & (\boldsymbol{mn})(\boldsymbol{nn})^{-1} \end{bmatrix}, \tag{A.8}$$

in which $\boldsymbol{n}$ and $\boldsymbol{m}$ are any two orthogonal unit vectors in the plane normal to the dislocation line $\boldsymbol{t}_{\psi}$. The Eigenvalues p_α of the matrix $\boldsymbol{N}$, found by solving $\boldsymbol{N}\boldsymbol{\xi}^\alpha = p_\alpha \boldsymbol{\xi}^\alpha$ for $\alpha = 1, 2, .., 6$, form complex conjugate pairs. Arranging the eigenvalues in such a way that p_4, p_5, p_6 are the complex conjugates of p_1, p_2, p_3 respectively and $\mathrm{Im}(p_\alpha) > 0$ for $\alpha = 1, 2, 3$, the corresponding orthonormal eigenvector $\boldsymbol{\xi}^\alpha$ can be split into two 3x6 matrices, i.e.

$$\boldsymbol{\xi}^\alpha = \begin{bmatrix} \boldsymbol{A}^\alpha \\ \boldsymbol{L}^\alpha \end{bmatrix}, \tag{A.9}$$

from which the components of the energy matrix **B** can be calculated as

$$B_{kj} = 2iL_{k\alpha}L_{j\alpha} \quad \forall \quad k, j, \alpha = 1,2,3. \tag{A.10}$$

Integrating equation A.7 over ψ for all the dislocation lines in the fan, the traction on the xy-plane at point P_1due to the dislocation fan is

$$\boldsymbol{n}^0 \cdot \boldsymbol{\sigma}^{\mathrm{f}}(r_1, \psi_1)|_{z=0} = \int_0^{\pi} \frac{\boldsymbol{B}(\psi) \cdot \boldsymbol{b}(\psi)\, d\psi}{2\pi r_1 \sin(\psi_1 - \psi)} \tag{A.11}$$

Substituting equations A.4 and A.11 into A.3 results in

$$\frac{1}{2\pi^2 \rho_1} \int_0^{\pi} d\varphi \, \frac{\left[\boldsymbol{C} \cdot \boldsymbol{m}_\varphi - (\boldsymbol{C} \cdot \boldsymbol{n}_\varphi)\left(\boldsymbol{n}_\varphi \boldsymbol{n}_\varphi\right)^{-1}(\boldsymbol{n}_\varphi \boldsymbol{m}_\varphi)\right] \cdot \boldsymbol{b_0}}{\sin(\varphi_1 - \varphi)} = \int_0^{\pi} \frac{\boldsymbol{B}(\psi) \cdot \boldsymbol{b}(\psi)\, d\psi}{2\pi r_1 \sin(\psi_1 - \psi)}, \tag{A.12}$$

for any point P_1 on the z=0 surface.

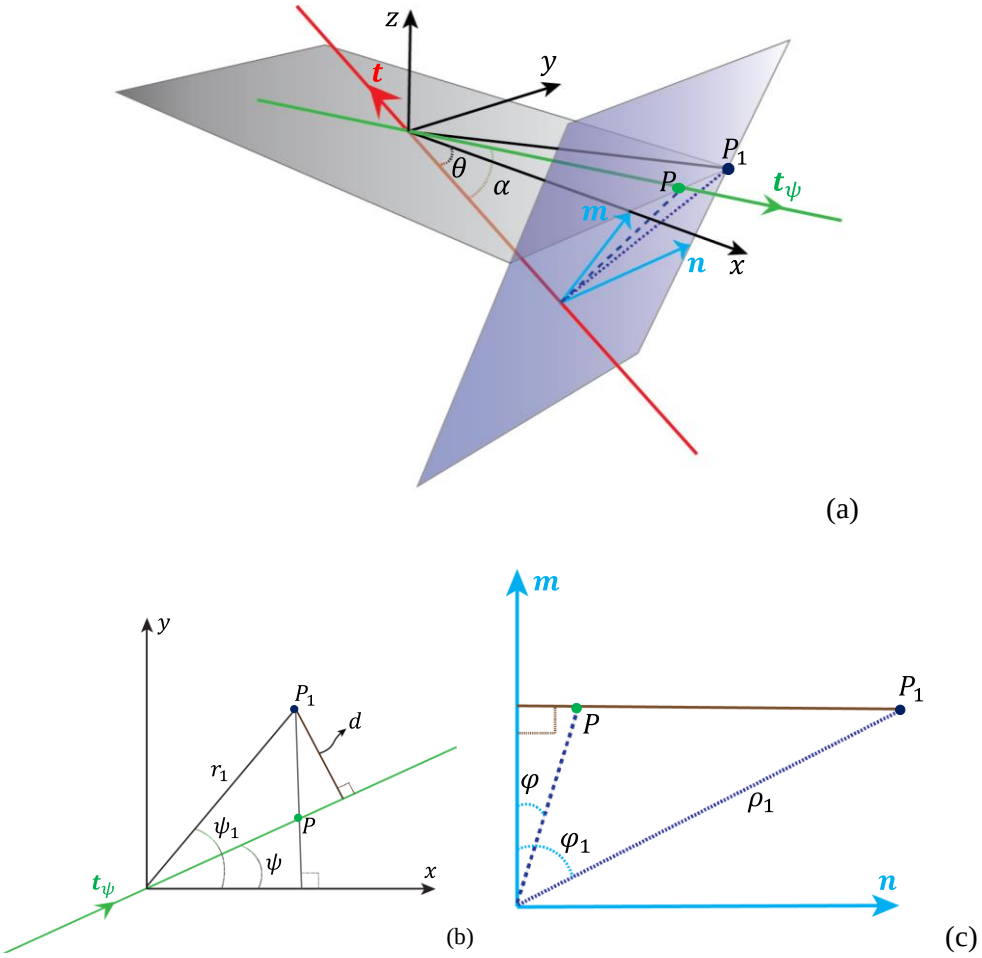

Figure 2-8. A point P_1 in the $z = 0$ plane is defined by the polar coordinates (r_1, ψ_1) in the xy-plane and (ρ_1, φ_1) in the $\boldsymbol{mn}$-plane. P is a point on a dislocation line t_ψ that lies at a polar angle ψ. *(b)* and (c) show the points P_1 and P in the xy and $\boldsymbol{mn}$ coordinates respectively

For any arbitrary point P located in the $z = 0$ plane, the relationship between its polar coordinates (r, ψ) in the global coordinate and (ρ, φ) in the local coordinate can be found from Figure 2-8(a) as

$$\rho = r \sin(\alpha) \tag{A.13}$$

and

$$\cot(\varphi) = \cot(\psi)\sin(\theta), \tag{A.14}$$

where θ is the angle between $\boldsymbol{t}$ and the x-axis while α is the angle between OP and $\boldsymbol{t}$. From equation A.14, we can derive that

$$d\varphi = \frac{\sin^2(\varphi)}{\sin^2(\psi)}\sin(\theta)\, d\psi = \frac{\sin(\varphi)\cos(\varphi)}{\sin(\psi)\ \cos(\psi)}\, d\psi \tag{A.15}$$

Based on figure A2(b) and A2(c), we also have

$$\frac{\sin(\psi_1 - \psi)}{\sin(\varphi_1 - \varphi)} = \frac{\cos(\psi_1)}{\cos(\varphi_1)}\sin(\alpha) \tag{A.16}$$

Substituting equations A.13-A.16 into equation A.12 and equating the integrands leads to the Burgers vector distribution of the fan,

$$\boldsymbol{b}(\psi) = \frac{\boldsymbol{B}^{-1}(\psi)}{\pi\sin(\alpha)}\left[(\boldsymbol{n_0 m_\varphi}) - (\boldsymbol{n_0 n_\varphi})(\boldsymbol{n_\varphi n_\varphi})^{-1}(\boldsymbol{n_\varphi m_\varphi})\right]\cdot \boldsymbol{b_0} \tag{A.16}$$

Chapter 3

INVESTIGATING THE RELATIONSHIP BETWEEN GRAIN ORIENTATION AND SURFACE HEIGHT CHANGES IN NICKEL POLYCRYSTALS UNDER TENSILE PLASTIC DEFORMATION

K Balusu, R Kelton, E I Meletis and H Huang

Submitted to Mechanics of Materials Journal in 2018[2]

[2]Copyright information: Elsevier, the publisher of Mechanics of Materials Journal, allows authors to include their articles in full in a dissertation

Abstract

This paper investigates the effect of the grain orientation on the surface roughening of nickel polycrystals undergoing plastic tensile deformation. Both experiment and simulation work was carried out. In the experiments, we measured the surface topography at different strain levels. The surface topography images were analyzed to classify individual grains as either rising or sinking. In simulations, we utilized a Crystal Plasticity Finite Element model that embeds a grain in an isotropic sample. This arrangement ensures that only the grain orientation of the embedded grain influences the grain surface topography. The average surface height of the grain was calculated for classifying its rising or sinking behavior. Both experiment and simulation results indicate that the grains with the loading direction close to the <001> and <111> lattice orientations tend to sink. In addition, a grain's loading direction orientation, and thus the Schmid or Taylor factor, does not uniquely determine whether it rises or sinks. The parametric study revealed that a grain's average surface height is contributed by the plastic deformation of the most stressed slip systems along the direction normal to the surface.

1. Introduction

Understanding material failure is essential for designing efficient structural components. Localized plastic deformation, which typically manifests as surface roughness changes, is considered as the start of material failure. Therefore, material failure may be predicted by monitoring the topography changes of the surfaces during the plastic deformation of ductile metals [1], [52]. Surface topography change is a result of the out-of-plane plastic deformation, which manifests itself due to the heterogeneity of the underlying microstructure in a polycrystalline metal. Therefore, understanding surface topography changes in relation to the underlying microstructure is crucial in predicting failure of metals.

Plastic induced surface roughening results from the formation of slip bands and the overall deformation of individual grains. The heights of the slip bands are usually small. As a result, their contribution to the surface topography changes is insignificant as compared to the overall deformation of individual grains [3]. Due to the anisotropic nature of grain crystals, individual grains with a unique crystal orientation display distinctive plastic and elastic behavior. Under plastic deformation, differently oriented grain crystals cause different out-of-plane deformations, leading to surface roughening. Grain-scale surface roughening can be classified into two categories based on the length scale, i.e., banding/ridging and orange-peel. For banding/ridging, clusters of grains having similar grain orientations and hence, similar surface heights, are organized into narrow bands. Orange-peel type roughness approximately maps the grain shape and is prominent in materials with random textures [53], [54]. The contribution of a grain's orientation to orange-peel type surface roughening is still unknown [55], [56].

Three main obstacles contribute to the difficulty in investigating the relationship between a grain's orientation and its surface changes. The first obstacle is that the neighboring grains, including the ones on the surface and underneath, could have a strong effect on the surface topography of the grain that is of interest [55], [57]. Sauzay (2006) has demonstrated that the onset of plasticity in a grain depends on the neighboring grains [58]. This neighboring grain effect exists typically over a few grain diameters. The inability to separate the effect of the grain's own orientation and that of its neighbor hinders the comprehension of the mechanism underlying the surface topography changes. Additionally, assessing the effects of the neighboring grains is complicated by the fact that the morphology and orientation of the subsurface grains are usually unknown.

The second obstacle is that the grain is usually characterized using simple factors such as the Taylor or Schmid factor [55], [56], [59]. The Taylor factor is calculated with the assumption that every grain in a polycrystal is constrained to undergo isotropic plastic deformation, i.e. isostrain.

The Schmid factor calculation assumes that the grain is completely unconstrained, and every grain experiences the same applied stress, i.e., isostress. Both these factors depend only on the grain's orientation in the loading direction. The traditional understanding of grain level sinking and rising is based on evaluating the 'hardness' of the grains, i.e., the ease of plastic deformation, based on one of these factors. For example, a large Taylor or a small Schmid factor implies that the grain is hard. Therefore, such a grain deforms less and rises relative to the average polycrystal surface. In contrast, a grain with a small Taylor or a large Schmid factor is soft and thus sink below the surface. However, the correlation between these factors and the surface topography changes is rather weak. Wouters et al. (2006) used the orientation imaging microscopy to investigate the relationship between the orientation of surface grains and their topography. They concluded that the Schmid factor of a surface grain alone is not sufficient to predict the evolution of the surface height. They hypothesized that a cumulative Schmid factor through the thickness would predict the depressions on the surface. Lee et al. (1998) only found a weak correlation between low Taylor factors and depressions on the surface. Similarly, Choi et al. (2004) also found a weak correlation between the valleys and low Taylor factors along with high Schmid factors. Both researchers attributed the discrepancy between theory and experiment to the influences of the in-plane neighbors and the subsurface grains on the surface topography changes.

The third obstacle is that it is difficult to simulate the surface roughening of a real-world sample using numerical simulation. Crystal Plasticity Finite Element Method (CPFEM) simulation has been extensively used to study the phenomenon of surface roughening under plastic strain [3], [4], [9]–[12]. CPFEM can produce reasonably accurate surface roughness changes, strain variations and evolution of orientation distributions averaged over a grain or a few grains [6]. However, studies attempting one-to-one correlation with experimentally observed surface roughening at scales smaller than grain dimensions has limited success [64], [65]. Zhao et al. attribute the discrepancy between simulation and experimental observations to the unknown grain boundary geometry

through the thickness direction [64]. Ha, et al. attribute the discrepancy to the inability in modeling plasticity near the grain boundaries [65].

This paper employs both three-dimensional surface profiling technique and CPFEM simulations to understand the influence of a grain's orientation on its own surface under plastic tensile load. Firstly, to minimize the effect of the neighboring grains, we characterize the measured height change of a grain with respect to its immediate neighbors. In simulations, we model the polycrystal as an anisotropic grain embedded in an isotropic frame. Secondly, instead of just using Taylor or Schmid factors, we use the grain's orientation for complete characterization. Lastly, to work with inaccuracies in numerical simulations, we evaluated a grain's behavior based on its relative surface height, classifying the grain as either sinking or rising. Only this rising or sinking behavior is used for comparing with experimental observations. This comparison confirms that the grains with an LD orientation near the <100> and <111> lattice always sink while grains with other LD orientations may rise and sink, indicating the ND orientation also play a role. Parametric studies were then carried out to understand how ND affects the surface height. Based on this study, we concluded that the ND orientation, not the Schmid or Taylor factor, determines the rising or sinking behavior for a grain with a specific LD orientation.

2.

Experiment

2.1. Methodology

The subsize tensile specimen was designed according to ASTM E8/E8M-13A, and its dimensions are given in Figure 3-1(a). The gauge length is 0.5 mm while the gauge width is 1.39 mm. A finite element analysis with isotropic material properties confirmed the constant stress state in the gauge area as depicted in Figure 3-1(b).

The sample was machined from as-received commercially available nickel 200 sheet with a purity of 99.52%. Both sides of the sample were polished with conventional sandpapers and alumina powders to an arithmetic average surface roughness R_a < 20 nm. After mechanical polishing, one side of the sample is electropolished in standard Struers A2 solution followed by etching in ASTM E407 - 25 solution to reveal the grain boundaries. The as-received material had a thickness of $1.575\ mm$, which was reduced to $1.17\ mm$ after polishing. The entire gauge area was imaged using Electron Backscatter Diffraction (EBSD) and then used to determine the orientation of every identified grain on the surface. The EBSD measurement confirmed a random distribution of grain orientations. The grain size, measured as per ASTM E112-13 planometric procedure, is 0.1 mm.

The sample was then loaded using a mechanical testing machine (Bose LM2 test bench). We measured the sample surface heights at three stress levels, i.e., at (a) 1.02, (b) 1.17, and (c) 1.3 times of the yield stress. Applied stress on the gauge section was calculated using the force applied as measured from the load cells of the tensile machine and the smallest cross-section area of the sample. The axial strain of the gauge section was not directly measured but approximated by fitting the slope of the stress-strain curve in the elastic region to be Young's modulus of nickel ($200\ GPa$). From this stress-strain curve, the three stress levels at which the sample is profiled correspond to applied axial engineering strains of (a) 0.75%, (b) 1.12%, and (c) 1.5%. The surface profiling was carried out using a Scanning White Light Interferometer (SWLI, Bruker NPFLEX). The mechanical testing machine was integrated with the SWLI microscope so that surface profiling can be performed without removing the sample from the mechanical tester.

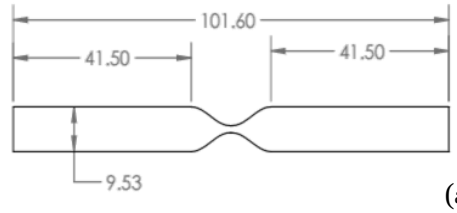

(a)

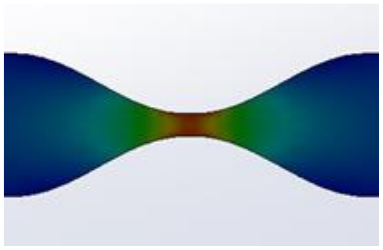

(b)

Figure 3-1. (a) Schematic representation of the tensile specimen. The gauge width is 1.39 mm, the length is 0.5 mm and the thickness is 1.17 mm; (b) FEM simulation showing uniform stress state in the gauge area. The loading direction is towards the horizontal.

2.2. Data analysis & results

Figure 3-2(a) depicts the SWLI surface topography image of the initial sample surface before loading. It reveals that the initial sample surface had a significant height drop of 4 μm at the edges, likely due to the rounding of the edges during polishing. For this reason, we exclude data acquired at locations that are within 200 μm from each edge. To remove the inherent curvature of the polished surface, we divided the gauge area into three equal vertical sections with around 20% overlap, applied curvature filtering to each section, and then stitched them back. (b-d) show the filtered surface topography at the three loading levels. These measurements clearly show that the sample surface developed significant surface roughness as the sample undergoes plastic deformation. It is worth pointing out that the out-of-plane displacements of individual grains appear to contribute to the majority of the surface topography changes. In addition, while the out-of-plane displacements of individual grains increase in amplitude with the increase of the applied stresses,

the direction of the out-of-plane movement, i.e. whether a grain sinks below or rises above the surface, does not change with the applied stress.

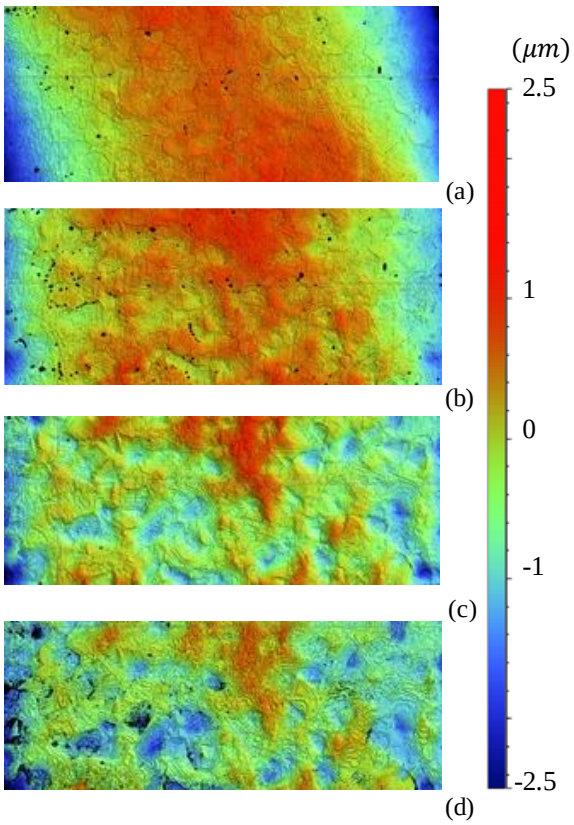

Figure 3-2. Surface topography images of gauge area showing the surface height distribution; The initial sample surface (a) and at an applied strain of (b) 0.75 %, (c) 1.12 %, and (d) 1.5 %. The applied load is along the vertical direction.

Figure 3-3 takes a closer look at the surface topography of a few grains and its surroundings to identify characteristic features of the deformed surface topography. The first observation is, clear orange-peel type roughness is noticeable, i.e. the surface topography features roughly conform to the shape of the grains. For some grains, the entire surface may rise above or sink below the surrounding surface, as shown in Figure 3-3(a) & (b). Other grains, however, may sink in some

portion of the surface and rise in the other, as shown in Figure 3-3(c). A small percentage of grains also developed slip bands. However, the surface heights of slipbands are much smaller in magnitude as compared to the overall surface height of the grain, as shown in Figure 3-3(d). Therefore, our study will be focused on the relationship between the grain orientation and the overall surface height of the grain.

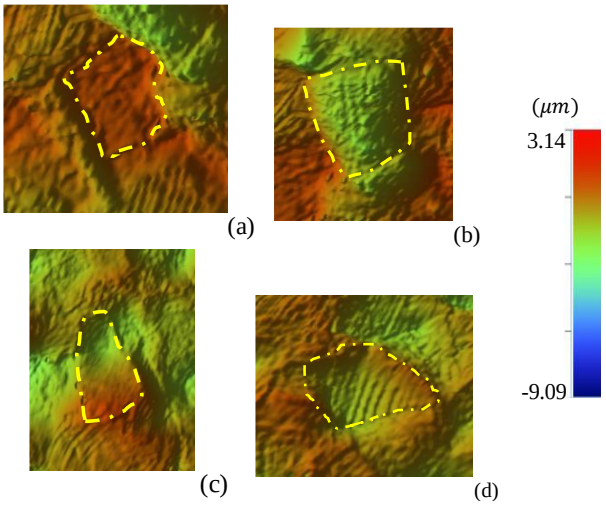

Figure 3-3. Surface at an applied strain of 1.5% showing a (a) rising grain, (b) sinking grain, (c) grain with both rising and sinking regions and (d) grain with prominent slipbands. The grains are identified by the dashed outline.

The surface of every grain is quantified by using a single parameter, the average surface height. For each grain, we assigned a square-shaped neighborhood that has a length of three times the grain's diameter and has the grain's centroid as its center. We then calculate the average surface height of the grain of interest and the neighborhood. Using these two parameters, a grain is classified to be either rising or sinking only if the grain's average height differs from that of its neighborhood by more than 10% of the root mean square (RMS) of the entire gauge surface height. The average surface height of the neighborhood is used as the reference because the grain-scale sinking, and rsing behavior is not captured when the average height of the entire gauge area is used. For example,

all the grains shown in Figure 3-4(b) have negative grain heights with respect to the average gauge height, indicating all the grains have sunk. However, the surface topography image shown in Figure 3-4(a) indicates that the grain of interest rose above its neighbors. Therefore, to classify a grain to be either rising or sinking, we use the grain's immediate neighborhood. This procedure leads to correct classification as shown for a grain in Figure 3-4.

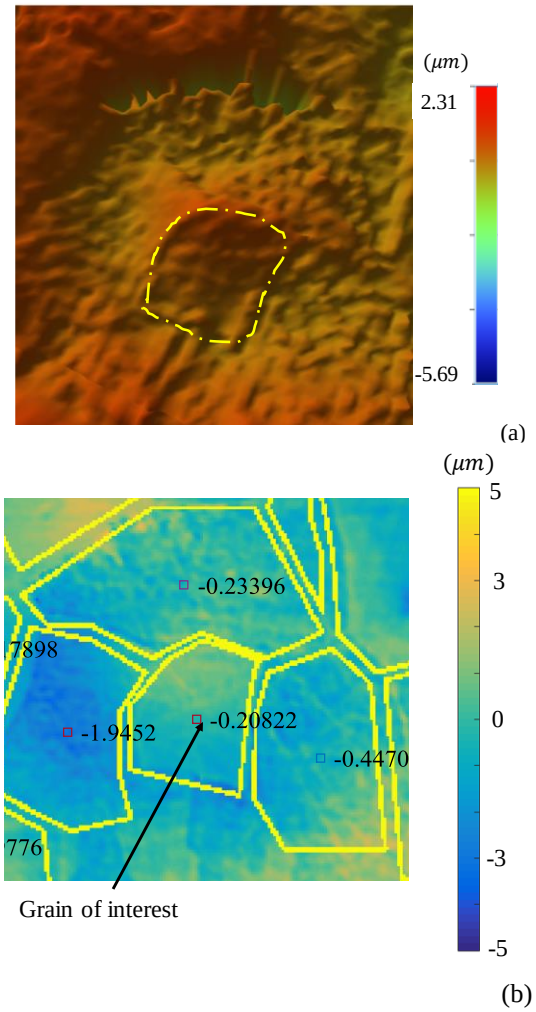

Figure 3-4. Classifying a grain of interest as sinking or rising; (a) Grains are shown in a 3D surface plot, with the grain of interest identified; (b) The heights of the same grains with reference to the average height of the gauge area. The yellow lines represent grain boundaries.

We excluded the smallest and the largest grains from the classification procedure. We only classify grains that lie within two standard deviations from the average grain size. It is done so because these may show Hall-Petch type grain hardening, i.e. the yield strength of a grain is inversely proportional to the grain size. This kind of hardening causes the smallest grains to show little plastic deformation and rise irrespective of their orientation. Similarly, Hall-Petch hardening causes the largest grains to sink irrespective of their orientation.

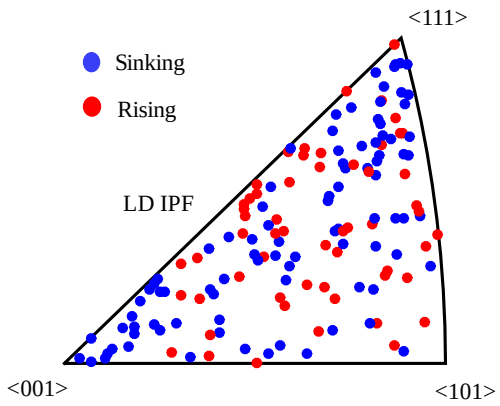

Figure 3-5. Distribution of grains classified as rising or sinking in the loading direction (LD) inverse pole figure (IPF) – Experiment.

Using the analysis procedure mentioned above, 150 grains in the gauge area are classified to be either rising or sinking from a total of 189 identified grains. The Inverse Pole Figure (IPF) in Figure 3-5 shows the lattice orientations of the rising and sinking grains along the loading direction (LD). IPF uniquely represents the crystal orientations in the LD because of the symmetry in face-centered crystals (FCC) like nickel. We used only the grain orientations in the loading direction because the Schmid and Taylor factors can be uniquely determined from these orientations. Based on the observations, we divided the IPF into three regions, i.e., near IPF vertex <001>, near IPF vertex <111>, and the rest of the IPF. We term 'near' as less than a vector distance of 0.15 from the vertex. The percentage of the sinking grains in these three regions are given in Table 3-1. 91.3% of

the grains sunk in the region near vertex <001> while 78.1% of the grains in the region near vertex <111> sunk. For the grains in the rest of the IPF, there is no preference for sinking or rising. Another observation is that the adjacent grains displayed dissimilar out-of-plane movements, i.e., one rises and the other sinks. It is worth noting that the grains displayed similar behavior at all three strain levels characterized.

Table 3-1. Percentage of grains sinking – experiment

Region	Near <001>	Near <111>	Rest of the domain
Sinking	91.3%	78.2%	51.6%

3. Simulation

To validate the observed grain orientation-surface height relationship, we performed studies on the surface height change of grains with different grain orientations using crystal plasticity finite element method (CPFEM).

3.1. Simulation setup

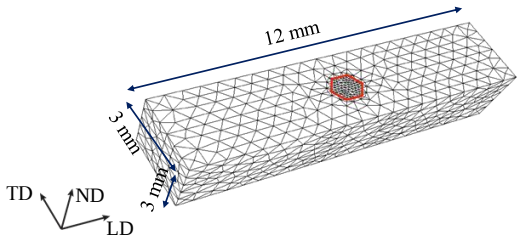

Figure 3-6. Finite element model with a grain embedded in an isotropic solid. The embedded crystal has a hexagonal face with an area of $0.866\ mm^2$ and has a depth of $1\ mm$.

Figure 3-6 shows the simulation model for the parametric study. It consists of a cuboid, with a length of 12 mm in the loading direction (LD), and a cross-section of 3X3 mm^2. A grain of a selected orientation is embedded in the center of the cuboid. The embedded grain is columnar with

a hexagonal face of $0.866\ mm^2$ in area and a depth of $1\ mm$. The face of the grain is chosen to be hexagonal to avoid straight edges thereby representing a more generic model. The embedded crystal is small enough so that its orientation does not affect the bulk behavior of the entire sample. It is also located in the center of the face, sufficiently far from sample edges. Anisotropic crystal plastic behavior, modeled using CPFEM, is used only for the embedded grain. The rest of the sample surrounding the grain was modeled using isotropic plasticity. We use the isotropic plasticity model for the surrounding material to ensure that it has no exaggeration on the behavior of the embedded grain but only an averaged behavior. More importantly, this model enables us to study whether the orientation of a grain alone can determine its rising or sinking behavior, regardless of the orientation of its neighbors.

The model generation and meshing were performed using NEPER software [66]. In the simulations, we stretched the sample along the LD up to a reasonably small strain of 5% at a strain rate of $2 * 10^{-5}\ s^{-1}$. Results are analyzed at few levels of applied strain that include levels comparable to experiments. In this work, the normal direction (ND) is the direction normal to the free surface of the embedded grain and the transverse direction (TD) is normal to LD and ND.

3.2. Material model

Assuming crystal slip is the dominant mechanism of plastic deformation, a crystal's plasticity is anisotropic. This anisotropy depends on the orientation of the specific slip systems relative to the fixed sample coordinates. Such a plastic deformation mechanism can be modeled using finite elements termed the Crystal Plasticity Finite Element Method (CPFEM), which ensures equilibrium of stresses and compatibility of strains. The formulation of this method is summarized in the appendix.

CPFEM was implemented using the DAMASK user-defined subroutines in ABAQUS standard solver [67] with the material parameters given in Table 3-2. These plasticity parameters

are empirical and were selected so that the simulated stress-strain graph of the polycrystalline sample under tensile loading matches that from the experiment [68], as shown in Figure 3-7. This simulation procedure to determine material parameters uses a cuboid (12x3x3 mm) with a random distribution of orientations for every mesh element as the sample. The mesh consists of 18,000 tetrahedral elements. The experimental sample and procedure were described in section 2.1. The curves start to deviate after 2% strain because the simulation fails to model necking and subsequent failure. This is acceptable since we limit our study to small amounts of deformation prior to necking. Also, since the experimental and simulation samples are different, the parameters are only approximate. The parameters for the isotropic plasticity model [69] were also chosen so that it results in the same axial stress-strain plot shown in Figure 3-7.

Table 3-2. Material parameters of nickel used in the CPFEM simulation

$\dot{\gamma}_0$	$10^{-3}\ /s$
m	0.02
Initial τ_c^{α}	128 MPa
τ_s	218 MPa
h_0	585 GPa
a	1
C_{11}	247 GPa
C_{12}	147 GPa
C_{44}	125 GPa

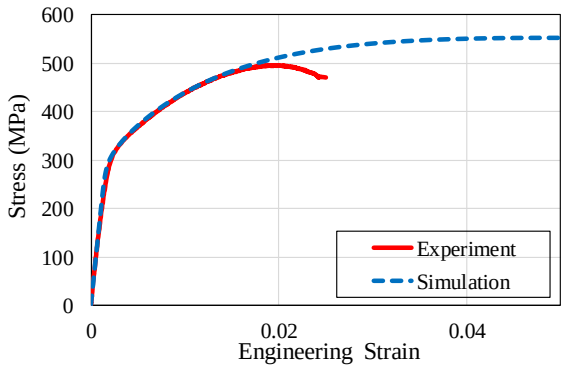

Figure 3-7. Simulated and measured stress-strain curves of a randomly textured polycrystal under tensile deformation.

3.3. Data analysis, results & discussion

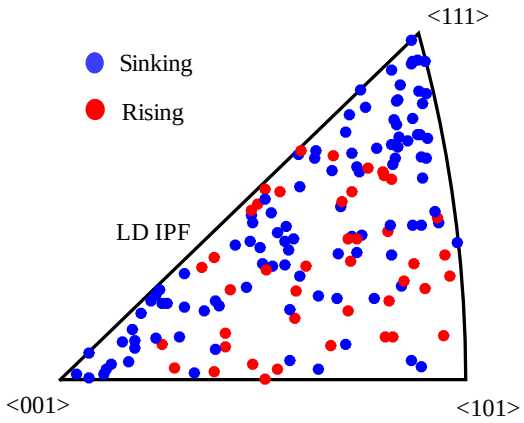

Figure 3-8. Distribution of grains classified into rising or sinking in the loading direction (LD) inverse pole figure (IPF) - simulation. Grain orientations are taken from the experimental sample.

The orientations of the 150 grain identified in the experiment as either rising or sinking were used in the simulation model described above. We characterized the out-of-plane displacement of the grain using the average height difference between the embedded grain and the isotropic surface. A grain with a negative average height difference is termed to be sinking and vice versa.

To compare with the experiment results in section 2, the LD orientation of the rising and sinking grains obtained from the simulation are plotted in the IPF shown in Figure 3-8, and the percentages of grains sinking in the three regions are given in Table 3-4. The simulations show that 91.3% of grains near vertices <001> sink while 96.9% of grains near <111> sink. About half of the grains (56.8 %) in the rest of the IPF, sink. These results qualitatively matched with the experimental observation, i.e., the majority of grains near <001> and <111> sink while the grains in the rest of the IPF have no preference for rising or sinking.

Table 3-4. Percentage of grains sinking - simulation

Region	Near <001>	Near <111>	Rest of the domain
Sinking	91.3%	96.9%	56.8%

Table 3-3. Percentage of grains with behavior deviating between experiment and simulation

Region	Near <001>	Near <111>	Rest of the domain
Deviation	8.7%	25%	48.4%

The percentage of grains whose behavior differs between simulation and experimental observations is given in Table 3-3. The simulations correctly predict sinking behavior for most of the grains near vertices <001> and <111> of the LD IPF. However, simulated behavior for half of the grains away from the vertices <001> & <111> differs from experimental observations, indicating that simulation prediction is almost random. We believe that the discrepancy is because the simulation treats the surrounding grains as isotropic and homogeneous material. In an actual polycrystal, the deformation of these neighboring grains is likely to be anisotropic and heterogeneous. In other words, the rising or sinking classification of the grains near IPF vertices

<001> and <111> are less influenced by the surrounding neighbors compared to the rest of the grain orientations. Despite the deviations, the simulations confirm the experimental observation that grains next to each other in the LD IPF could show opposite behaviors (i.e., one of them sinks and the other rises). This observation implies that the LD lattice orientation doesn't uniquely determine the rising or sinking behavior of grains in most of the cases. For a grain's orientation to be uniquely specified, lattice orientations in two mutually perpendicular directions are necessary. In grain orientation mapping using EBSD, lattice orientations in LD and ND, which are perpendicular to each other, are generally specified. Therefore, to determine whether a grain will rise or sink under plastic deformation, we believe the grain orientation towards the free surface (ND) also needs to be considered.

4. Parametric study of the effect of the normal direction lattice orientation on the surface height changes of grains

To gain a better understanding of how exactly the ND orientation of a grain influences its surface height, we carried out parametric studies by varying the ND orientation of a few grains having representative LD orientations. Figure 3-9(a) shows one of the LD orientations used and its corresponding ND orientations. For a given LD, ND could be any direction lying on the plane normal to it. Therefore, we first choose a specific ND orientation and construct nine more ND orientations by rotating the ND about the LD by 180° in equal size intervals. Due to symmetry, a range of 180° is sufficient to represent all ND orientation possibilities. Figure 3-9(b) shows the IPF with 15 representative LD orientations, each assigned with a number, used in our study. These LD orientations were chosen to be spread out over the entire domain to represent grains with randomly distributed LD orientations. For these LD orientations, the first ND orientations are along the {001}-{101} line and are termed as Set-I NDs, as shown in Figure 3-9(c). In total, we simulated 150 different orientations for the embedded grain.

4.1. Orientation setup

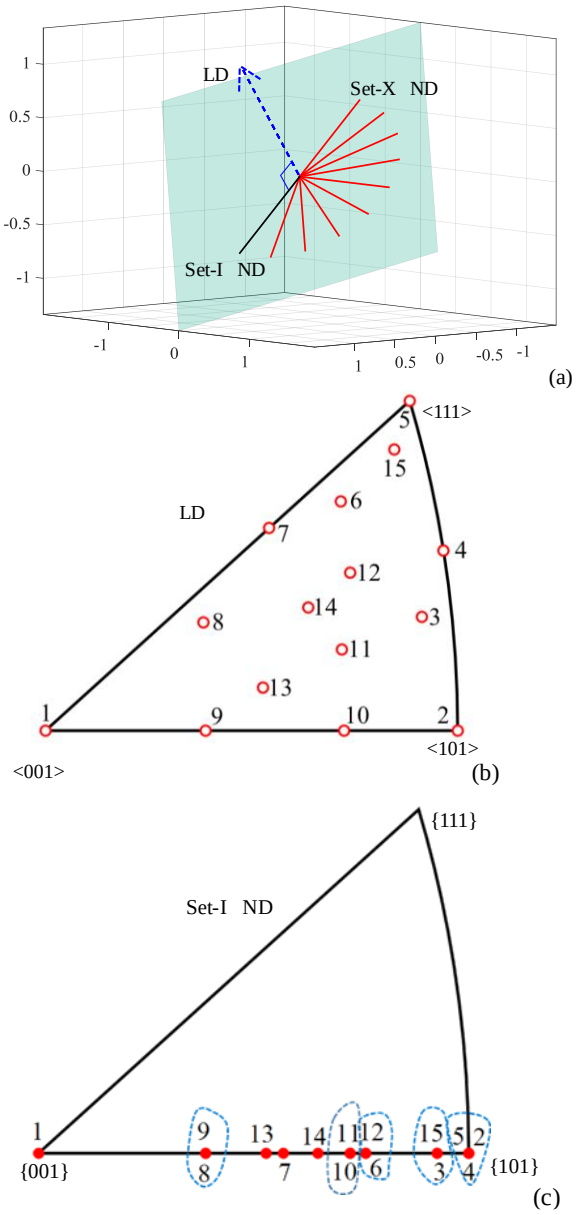

Figure 3-9. *(a)* Representing the grain orientation in a lattice coordinate space. For a particular loading direction (LD), 10 normal directions (ND), evenly distributed over 180^{o}, are used for parametric study; *(b)* Inverse Pole Figure (IPF) shows the LD orientations of the 15 grains used. (c) Set-I ND orientation for each LD orientation.

4.2. Results & discussion

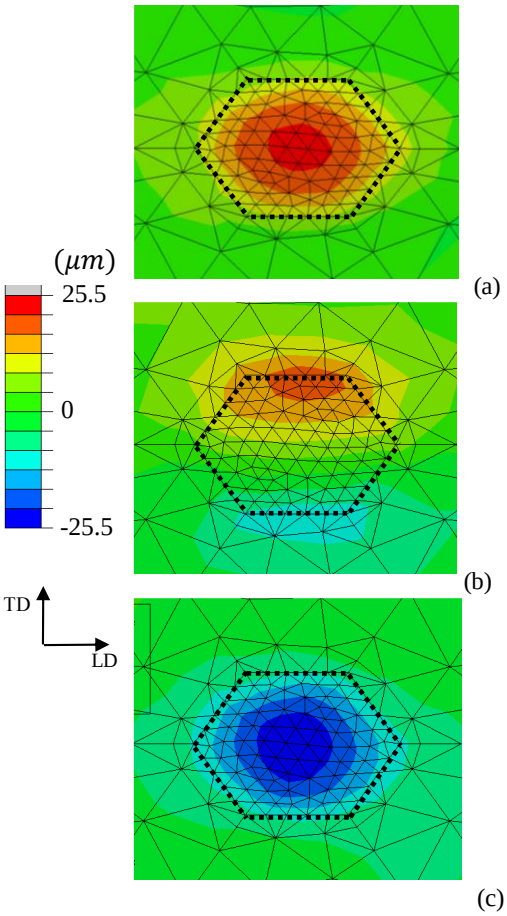

Figure 3-10. Surface heights of grain with loading direction (LD) orientation No. 2. The normal direction (ND) orientation is rotated from Set-I ND orientation by (a) 0° (b)40° and (c) 90°. The embedded grain is outlined by the dotted line.

Figure 3-10 shows the simulated surfaces of three grains with the same <101> LD orientation and three different ND orientations, i.e., Set-I ND, ND rotated by 40° and ND rotated by 90°. For the Set-I ND orientation, the surface of the entire grain rises relative to the surrounding material, as shown in Figure 3-10(a). When the ND orientation is rotated by 40°, a portion of the

grain rises, and a portion sinks, as shown in fig. 10(b). When the ND orientation is rotated by 90°, the entire grain sinks below the surrounding material (Figure 3-10(c)).

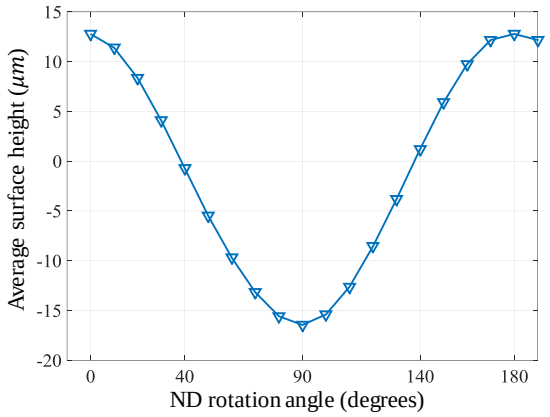

Figure 3-11. Averaged grain surface heights of grain with loading direction (LD) orientation No. 2, plotted over all normal directions (ND). Angle 0° represents set-I ND.

We followed the procedure described in section 3.3 to calculate the average grain surface height for each grain orientation from the simulation results. Figure 3-11 shows the variation of the average surface height with the ND orientation for grains with the LD orientation at <101> IPF vertex. The average surface height is the highest at 0°, i.e., Set-I ND orientation, reduces to zero when the ND orientation rotated by about 45°, and reaches the lowest value when the ND orientation is rotated by 90°. Looking at the behavior for all the ND orientations, the variation is sinusoidal and has a period of 180°.

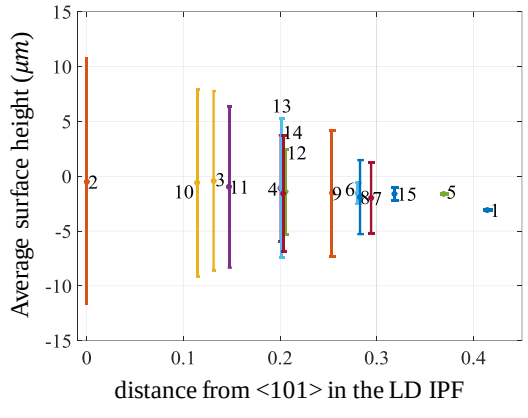

Figure 3-12. Average grain surface heights of all grains at an axial deformation of (a)5 %, and (b)1%. The range of height variations for grains with the same loading direction (LD) orientation are plotted as vertical bars.

Figure 3-12 shows the average surface height results from all 150 simulated grain orientations. In this figure, each vertical bar represents the range of the average heights for grains having the same LD orientation but varying ND orientations. The height of the bar is equal to the difference between the largest and smallest average height of all the grains with the same LD orientation. The x-axis of Figure 3-12 was chosen to be the distance from vertex <101> of the LD IPF because it is the simplest quantity that gives a rough trend of decreasing height variation. We

observed that the variations of the average height for grains with different LD orientations could be categorized into three groups. Group #1 contains the grains with the LD orientation near <101> vertex i.e. LD orientation No. 2. Grains in this group can rise or sink, depending on their ND orientation. The variation of the average height among this group is the largest for all the LD orientations. Group #2 includes the grains with their LD orientation near vertex <001> and <111>, i.e. the LD orientation 1, 5, 15. The average height of these grains varies marginally as the ND orientation changes. Also, these grains always show negative average surface heights, i.e., their surfaces always sink.

Group #3 contains the rest of the selected grains with LD orientations far from the vertices of the IPF. These grains can also rise or sink depending on the ND orientation. However, the variations of the average height are smaller than those in group #1. It is also worth mentioning that the observations just made don't change with applied strain. Figure 3-12(a) and (b) show results from the applied axial strain of 5% and 1% respectively. Only the magnitude of variation in the average height increases with the applied strain. Therefore, we only discuss results at 5% applied axial strain from now on.

The simulation results are consistent with the previous observation that the grains with the LD orientations away from LD IPF vertices <001> and <111> can either rise or sink. Thus, the parametric simulations confirm that the LD orientation is not a unique factor in determining the sinking and rising of the grains in group 2 or 3. For the grains in group #1, however, whether the grain rises or sinks can be determined from their LD orientation alone.

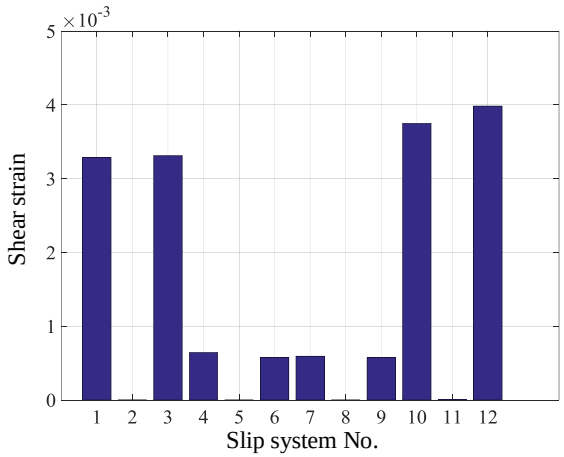

Figure 3-13. Accumulated shear strain on each of the 12 slip systems for a grain with loading direction (LD) orientation No. 2 and Set-I normal (ND) - simulation.

To explain the variation in the average height with the ND orientation we examine the slip systems. From the CPFEM simulations, we extracted the shear rate of every slip system, as given by equation 4, at integration points in every mesh element. Integrating shear rate values over each time step of the simulation determines accumulated shear strain. These values are then averaged over the entire grain. First, we look at the slip systems of the grains with LD orientation at the <101> IPF vertex, which displayed the most variation in average surface height. Figure 3-13shows the average shear strain values for each of its 12 slip systems. The accumulate shear strains shown is for the Set-I ND orientation since we observed that the influence of the ND orientation change is insignificant. The slip systems are numbered such that slip system No. 1 to 3 are on the same slip plane, 4 to 6 are on the second slip plane and so on for each of the four slip planes. We see that slip is accumulated almost equally on four slip systems and is negligible on the others.

The deformation of this grain contributed by the four active slip system can be calculated using strain transformation, assuming the strains are small and lattice rotations are negligible [70]. Since the normal strains along that ND and LD are proportional to the shear strain on the slip plane,

normalizing these two strain components results in a parameter that is independent of the shear strain. Figure 3-14 shows the normalized strain along the ND, i.e. $d\varepsilon_{ND}/d\varepsilon_{LD}$ contributed by each of the four slip systems. For each slip system, the normalized ND strain varies with the ND orientation in a sinusoidal pattern with a period of 180°. The curves from each of the slip systems are the same in amplitude but two of the slip systems vary in 'phase'. In other words, the ND orientation locations of the peak strains are different for two of the slip systems. Assuming all four slip systems have the same amount of slip, i.e. the shear increment is the same for all four slip systems, the total ND strain is the linear superposition of the ND strain contributed by each slip system. The resulting $d\varepsilon_{ND}/d\varepsilon_{LD}$ ratio is shown as the blue dashed line in Figure 3-14. When the ND rotation angle is zero, i.e. the grain has the ND orientation $\{10\bar{1}\}$, the $d\varepsilon_{ND}/d\varepsilon_{LD}$ ratio is zero. In other words, a crystal of this particular orientation has zero strain along the ND when it is strained in the LD. Considering that the sum of the three normal strains always remains zero in plastic deformation, strain in the TD for this case would be negative of the strain LD. If the ND orientation is rotated by 90°, the strain in the ND is the negative of LD strain and the TD strain is zero. In this case, the TD orientation is along $\{10\bar{1}\}$. Therefore, the normal strain or the dimension change in the $\{10\bar{1}\}$ crystallographic direction is always zero for grains with <101> LD orientation. The same observation has been previously reported by Kalidindi and Anand [71] from experiment and simulation of a single crystal with a circular cross-section under compression. They explained this observed by stating that a direction that is normal to the slip direction and lies on the slip plane does not have dimension change when materials deform through slip. Grains with the <101> lattice orientation in the LD have two active slip planes, each having two slip directions. The resultant of the slip directions on each slip plane is normal to the $\{10\bar{1}\}$ crystallographic direction, which also lies on the slip planes. As such, the $\{10\bar{1}\}$ direction has no dimension change, as confirmed by Figure 3-14**Error! Reference source not found.**.

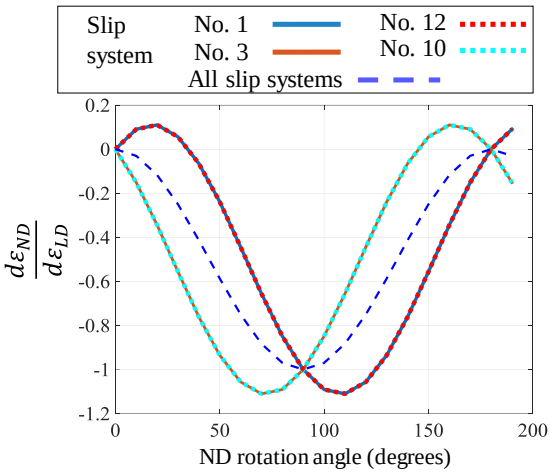

Figure 3-14. Normal strain increment ratios as a function of the ND orientation for grains with <101> loading direction (LD) orientation – theoretical prediction.

The deformation behavior from the four activated slip systems can explain the effect of ND orientation on the surface topography change show in Figure 3-10& Figure 3-11. Based on Figure 3-14, a crystal with the Set-I ND orientation does not show any normal strain the ND. On the other hand, the surrounding isotropic material deforms in ND. As a result, the grain rises the most relative to the surrounding isotropic material (Figure 3-10 (a)). Similarly, if the ND orientation is rotated by 90°, the dimension change towards the ND is negative and greatest. As a result, the grain sinks the most relative to the surrounding isotropic material (Figure 3-10 (c)). When the ND orientation is rotated by about 45°, the $\{10\bar{1}\}$ crystallographic direction is oriented at the diagonal direction. Since the dimension along this direction does not change, the dimension along the other diagonal direction must reduce the most. As a result, one portion of the grain surface rises and the other sinks (Figure 3-10(b)).

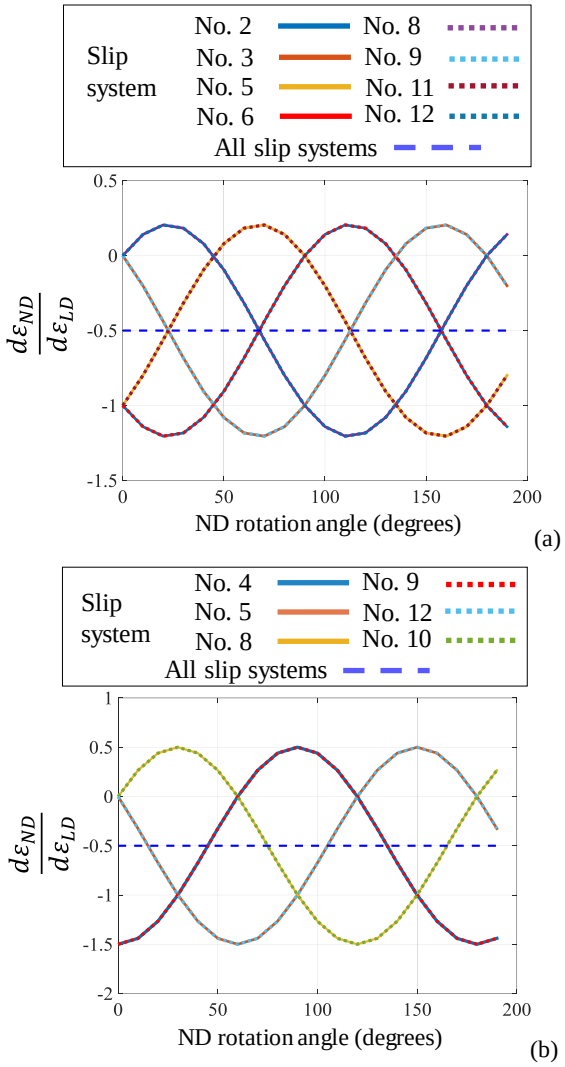

Figure 3-15. Normal strain increment ratios as a function of the ND orientation for grains with (a) <111> and (b)<001> loading direction (LD) orientations – theoretical prediction; (a) Six active slip systems with three of them same as the other three; (a) Eight active slip systems with four of them same as the other four.

For the grains with <001> and <111> LD orientations, the simulation shows that eight and six slip systems are activated, respectively. For the grain with <001> LD orientation, the $d\varepsilon_{ND}/d\varepsilon_{LD}$

curves contributed by the eight slip systems have the same amplitude but have four different phases, as shown in Figure 3-15(a). In other words, there are four distinct pairs of curves. Similarly, the six activated slip systems in the grain with <111> LD orientation have three pairs of distinct $d\varepsilon_{ND}/d\varepsilon_{LD}$ curves with three different phases, as shown in Figure 3-15(b). The resulting deformation from all these slip systems is a constant $d\varepsilon_{ND}/d\varepsilon_{LD}$ of -0.5 for both grains. This implies that the deformation is isotropic. That is why these grains show no variation of the surface height with change in the ND orientation.

To understand the deformation behavior of the grains with LD orientations away from the vertices of the IPF, we use the grains with LD orientation No. 11 as an example, since it is at an approximately equal distance from the three IPF vertices. Figure 3-16(a) shows the shear strain on each of its twelve slip systems. In this case, just one slip system dominates the shear strain, which is labeled as No. 10. The red curve in Figure 3-16(b) shows the $d\varepsilon_{ND}/d\varepsilon_{LD}$ curve for the deformation from this dominant slip system. The curve in black represents the average surface height variation with the ND orientation, extracted from the simulation results. The phases of these two curves are slightly different. In addition, the amplitude of the $d\varepsilon_{ND}/d\varepsilon_{LD}$ red curve is the same as the net $d\varepsilon_{ND}/d\varepsilon_{LD}$ curve for the grains with <101> LD orientation (see Figure 3-14). However, the height variation here is less than that for grains with the <101> LD orientation. These discrepancies in phase and amplitude indicate that the deformation of the grains with No. 11 LD orientation is not solely contributed by one dominant slip system. The other three slip systems i.e. slip systems 1, 9, and 12, which also show significant slip, may contribute to the deformation as well (Figure 3-16 (a)). When combined, they contribute as much shear strain as the dominant slip system. Figure 3-16(b) shows the $d\varepsilon_{ND}/d\varepsilon_{LD}$ curves from these three slip systems. These curves have different amplitudes and phases. Assuming the shear increments are proportional to the shear strains shown in Figure 3-16(a), the net $d\varepsilon_{ND}/d\varepsilon_{LD}$ contributed by all four active slip systems is shown as the blue dashed line in Figure 3-16(b). The phase of the net $d\varepsilon_{ND}/d\varepsilon_{LD}$ curve matches with that of the

average surface height curve. Moreover, the resultant of all the active slip systems has a lower amplitude. This explains why the surface height variation for this LD orientation is lower than that for grains with the <101> LD orientation.

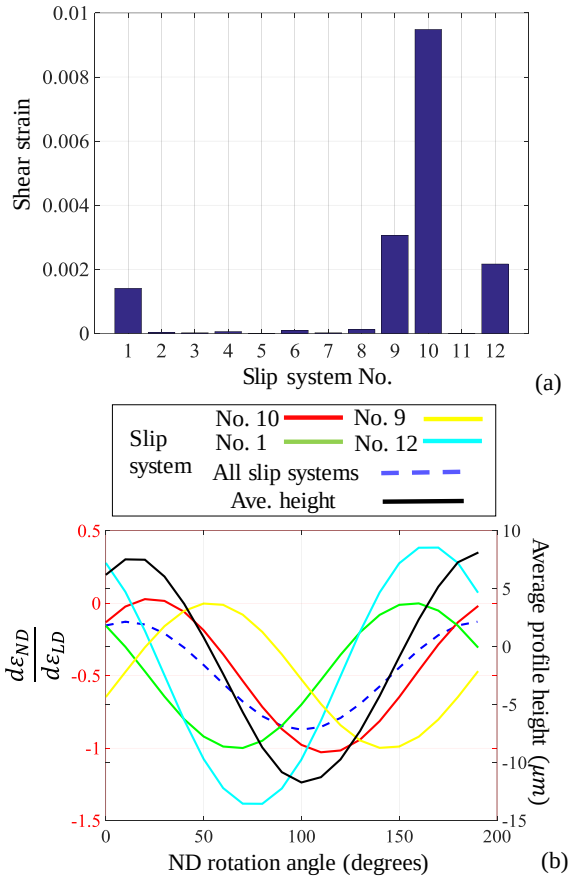

Figure 3-16. (a) Accumulated shear strain on each of the 12 slip systems for a grain with loading direction (LD) orientation No. 11 and Set-I ND, as calculated from the embedded grain simulation; (b) Normal strain increment ratios as a function of the normal direction (ND) orientation for grains with LD orientation No. 11 – theoretical prediction. The plot also shows the average surface height calculated from the simulation.

The slip of the active slip systems explains the surface-height variation with respect to the ND orientation for all three groups of grains we examined. To investigate why these specific slip

systems are activated, we calculate the Schmid factor of every slip system. Eight, six or four slip systems that are activated in grains with <100>, <111> & <101> LD orientations, respectively, also have the highest Schmid factors. For grains in the interior, however, only the dominant slip system was found to have the highest Schmid factor. In addition, the three other slip systems that also contribute to the height variation are those having the next highest Schmid factors. Therefore, the dominant and other active slip systems are determined by the Schmid factor. The same conclusion has been previously made through experimental observations of slip bands [56], particularly for grain orientations in the interior of the LD IPF.

The largest Schmid factor as well as the Taylor factor, both estimate the grain hardness, are a function of only the LD orientation. Most researchers believe that a hard grain rises while a soft grain sinks. With this assumption, the rising or sinking behavior of a grain can be uniquely determined from the LD orientation. However, both our experiment and simulation show that most of the grains with the same LD orientation i.e. the same Schmid and Taylor factor, may rise or sink depending on the ND orientation. Therefore, the value of Schmid or Taylor factor has no role in determining the grain surface height for most grain orientations. The only observation that can be explained by Schmid or the Taylor factor could be the sinking of the grains at <100> LD IPF vertex. The grains at LD IPF vertex <001>, often termed as the cube orientation, sink significantly more than the surrounding isotropic material (see Figure 3-12). The same observation has been previously made by other researchers [53], [55], [60], [72]. They explained that grains with the <001> LD orientation sink more because Taylor and Schmid factor predict these grains to be softer than the average polycrystal. However, the same explanation does not seem to be applicable for grains with <111> LD orientation. Taylor factor and Schmid factor predict these grains to be harder than the average polycrystal and hence they are expected to rise. However, in both experiments and simulations, these grains marginally sink (seeFigure 3-12). Therefore, Taylor and Schmid factor does not explain the surface topography behavior for these grains.

In summary, Schmid and Taylor factors calculated from the LD orientation do not uniquely determine the grain surface height, even though the LD orientation, through Schmid factor analysis, determines the active slip systems that contribute to the grain deformation. The combination of the deformation contributed by these active slip systems along the ND determines the grain surface height.

Conclusion

5. This study investigated the relationship between a grain's orientation and its average surface height in a nickel polycrystal during tensile plastic deformation. Both experimental surface profiling and crystal plasticity simulations were carried out. The significant conclusion is that a grain's hardness as estimated by Taylor or Schmid factors does not determine its surface height. It is the net deformation along with the ND orientation from a grain's most stressed slip systems, i.e., those with the largest Schmid factors, that determines whether a grain will sink or rise.

The presented work is intended to be the initial step to study the contribution of grain orientations to plasticity induced surface roughness. By neglecting the neighboring grains and focusing on an individual grain, we gained an understanding of the relationship between the orientation of a grain and its average surface height. For future work, we plan to investigate the effect of neighboring grains to explain deviations between experiment and simulations. This future study may also explain the localized surface topography changes as well.

Acknowledgments

This work has been funded by the Air Force Office of Scientific Research (AFOSR) grant FA9550-14-1-0319.

Appendix. Crystal Plasticity Finite Element method (CPFEM) **[8]**

The total deformation gradient tensor $\boldsymbol{F}$ at each integration point in every mesh element of the finite element model can be decomposed as

$$\boldsymbol{F} = \boldsymbol{F}_e \boldsymbol{F}_p \quad , \tag{3.1}$$

where $\boldsymbol{F}_e$ and $\boldsymbol{F}_p$ are elastic and plastic parts of the deformation gradient. The plastic deformation evolves as

$$\dot{\boldsymbol{F}}_p = \boldsymbol{L}_p \boldsymbol{F}_p \quad . \tag{3.2}$$

The plastic velocity gradient $\boldsymbol{L}_p$ is formulated as the sum of the shear rates $\dot{\gamma}^{\alpha}$ of all slip systems, i.e.

$$\boldsymbol{L}_p = \sum_{\alpha=1}^{12} \dot{\gamma}^{\alpha} \boldsymbol{m}^{\alpha} \otimes \boldsymbol{n}^{\alpha}. \tag{3.3}$$

$\boldsymbol{m}^{\alpha}$ and $\boldsymbol{n}^{\alpha}$ are the unit vector describing the slip direction and that normal to the slip plane of the slip system α, respectively. $\boldsymbol{m}^{\alpha}$ and $\boldsymbol{n}^{\alpha}$ are directions specific to the lattice structure and 12 sets exist in a FCC lattice such as nickel. The constitutive equations of the specific plastic slip model gives each shear rate $\dot{\gamma}^{\alpha}$ as a function of the external stress and the critical resolved shear stress.

In this paper, we used a phenomenological model of plastic slip [73], in which the critical resolved shear stress τ_c^{α} describes the plastic hardness for each slip system α. The power-law type kinetic behavior of a slip system that determines the shear rate $\dot{\gamma}^{\alpha}$ is

$$\dot{\gamma}^{\alpha} = \dot{\gamma}_0 \left| \frac{\tau^{\alpha}}{\tau_c^{\alpha}} \right|^{\frac{1}{m}} sgn(\tau^{\alpha}) \quad , \tag{3.4}$$

where the material parameters $\dot{\gamma}_0$ and m are the reference shear rate and the rate sensitivity of slip, respectively. The resolved shear stress of a slip system α is

$$\tau^{\alpha} = 0.5\, \boldsymbol{C}[\boldsymbol{F}_e^T \boldsymbol{F}_e - \boldsymbol{I}] : \boldsymbol{m}^{\alpha} \otimes \boldsymbol{n}^{\alpha} \quad , \tag{3.5}$$

where $\boldsymbol{C}$ is the elastic stiffness tensor of the material. The initial critical resolved shear stress τ_c^α is a material parameter, which is assumed to be the same for every slip system. The evolution of the critical resolved shear stress τ_c^α, i.e. the hardening behavior, is

$$\dot{\tau}_c^\alpha = \sum_{\beta=1}^{12} h_{\alpha\beta} \left| \dot{\gamma}^\beta \right| \quad , \tag{3.6}$$

The hardening matrix $h_{\alpha\beta}$ captures interactions amongst various slip systems and is given by

$$h_{\alpha\beta} = q_{\alpha\beta} \left[h_0 \left(1 - \frac{\tau_c^\beta}{\tau_s} \right)^a \right] \quad , \tag{3.7}$$

h_0, a and τ_s are the reference hardening rate, the hardening exponent, and the resolved saturation stress, respectively. These slips hardening parameters are assumed identical for all FCC slip systems. The parameter $q_{\alpha\beta}$ is a measure for latent hardening; its value is taken as 1.0 for coplanar slip systems α and β, and 1.4 otherwise, rendering the hardening model anisotropic.

Chapter 4

PRELIMINARY RESULTS FOR FUTURE WORK

We have made progress in the study of the relationship between grain orientation and the surface height. This chapter carries out preliminary investigation of two more aspects of grain-scale surface roughness formation. Section 1 focuses on the relationship between surface heights and strains, and stresses. Section 2 focuses on the effect of neighboring grains on a grain's surface height

1. The relationship between average grain-surface heights and plastic strains

The understanding of this relationship would help in the prediction of strain localization which could lead to the initiation of failure. Since, the surface roughness formation and deformation localization are both the result of the unique deformation of individual crystals; it is expected that they would be related. Assessing the current state of research, surface roughness formation relationship to the underlying stress and strain fields have been determined only in materials with dominant grain orientations [59]. The understanding of the relationship between a grains surface height and its orientation is still lacking.

In this section, the same simulations as in the previous chapter were used, but here, strains and stresses were extracted in addition to the surface heights.

1.1. Results and discussion

The grain-surface displacement data in the ND direction (i.e., surface heights) was extracted from the results of all the 150 simulations. We quantified the grain-surface height by calculating the average height difference between the embedded grain surface and the isotropic surface. Also, in each of these simulations, we extracted Green-Lagrangian plastic strains over the entire embedded grain. We extracted Green-Lagrangian strains in three directions: the loading

direction (LD), the normal direction (ND), and the transverse direction (TD). Figure 4-1 illustrates the average height plotted with respect to the grain-averaged plastic strains for all grain orientations. A unique color represents grains with the same LD orientation. Each subplot shows strains in a particular direction. Other strain components (shear strains) are not shown because they do not have a relationship to the average surface heights.

We can observe from Figure 4-1(a) that, for a specific LD orientation, even if the ND orientation change produces a surface-height change, the plastic strain in the LD remains the same. This implies that the LD strains are determined by the LD orientation and are not sensitive to the ND orientation of the grains. As a result, the LD strains are not correlated to the surface height. However, a linear relationship exists between the average height and the average plastic strains in both the normal (Figure 4-1(b)) and transverse directions (Figure 4-1 (c)). The average height is inversely proportional to the magnitude of the plastic strain in the ND and is directly proportional to the magnitude of the plastic strain in the TD. This opposite behavior indicates that strain variations in ND and TD are coupled. The consequence of the linear relationship is that a rough estimate of the strains in ND and TD directions can be made from just the average surface height irrespective of the grain orientation.

The explanation for this behavior is as follows. For all grains with the same orientation in the LD, the LD strains are the same, irrespective of the grain orientation in ND. To satisfy the condition of constant volume during plastic deformation, the grain should be shrinking in the directions normal to LD. However, this deformation in the plane of the cross-section is non-uniform, that is, it is different in ND and TD. This non-uniformity depends on the activated slip systems. Now, when the crystal orientation of LD is changed, the deformation in TD and ND, reflected as plastic strains, also change. For this reason, when the strain in one direction decreases, the strain in the other direction increases.

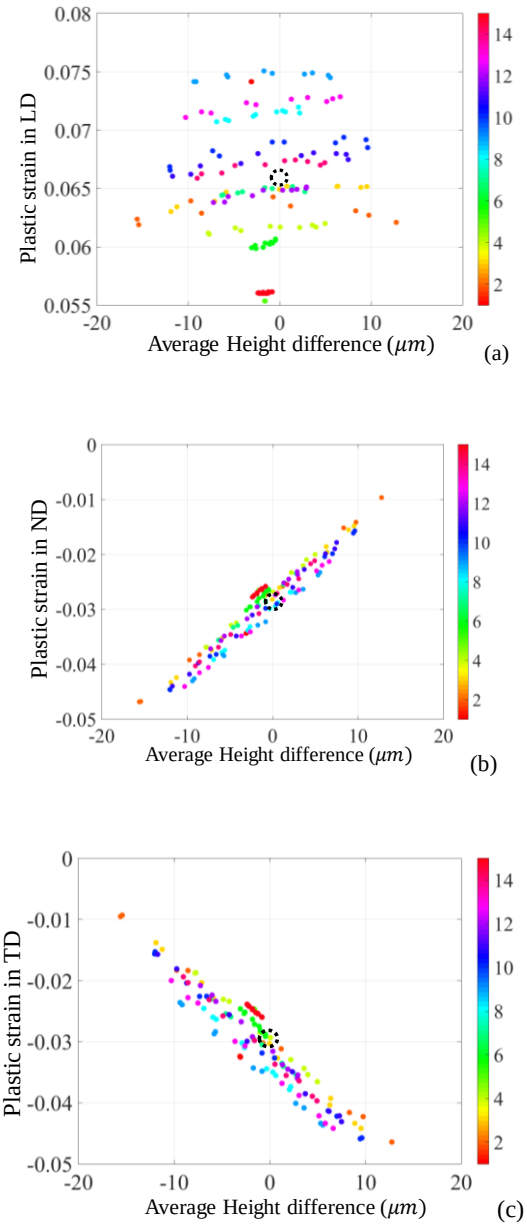

Figure 4-1. Plastic strains in (a) the loading direction (LD), (b) the normal direction (ND), and (c) the transverse direction (TD) averaged over the entire grain and plotted with respect to the average surface height. Results from all the grain orientations are shown, and each color represents the grains with the same LD orientation (Nos. 1-15), indexed by the colorbar. The dotted circle represents the strains in an isotropic material.

Another observation is that the overall variation in the plastic strain in LD (0.02) is much less than the variation in the plastic strain in ND or TD (0.04). The variation in the LD plastic strain for grains with different LD orientations, even though small, reflects in the strains in TD and ND. In Figure 4-1(a), grains with orientation No.15 (the group of red data points in the bottom) have the smallest plastic strain in LD. As a result, these grains show slightly less strain magnitude in ND and TD for the same grain height when compared to the other grains, as observed in Figure 4-1(b & c). Note that from LD strain can be determined if the strains in TD and ND are known under the assumptions of constant volume in plastic deformation. Since the determination of TD and ND plastic strain from the surface height is only an estimate, and the differences in strains in the LD are small, LD strain cannot be determined using LD and TD plastic strains either.

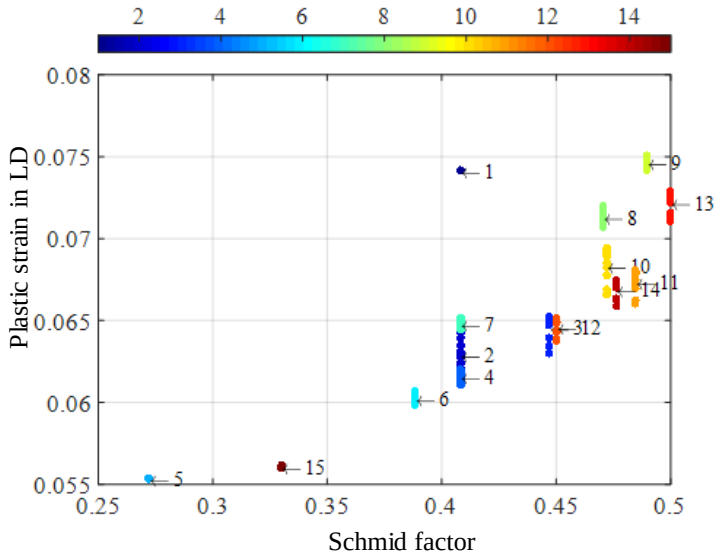

Figure 4-2. Variation of the plastic strain in the loading direction shown with respect to the

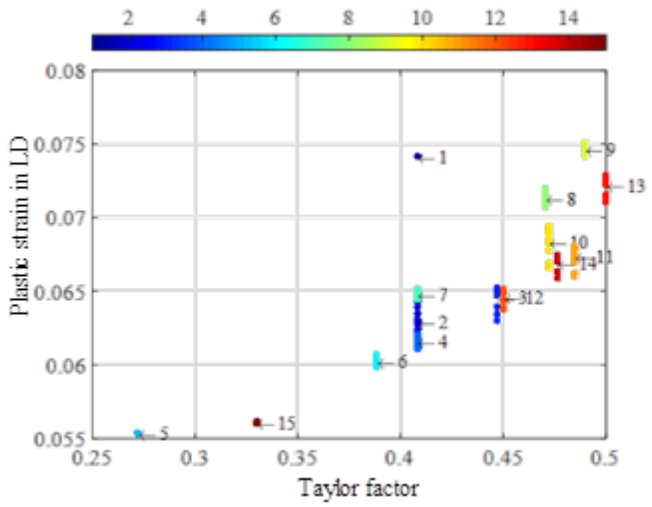

Figure 4-3. Variation of the plastic strain in the loading direction with respect to the Taylor factor.

Figure 4-2 shows the average plastic strain in the loading direction plotted with respect to the Schmid factor for all grain orientations. Figure 4-3 shows the average plastic strain in the loading direction plotted with respect to the Taylor factor for all grain orientations. These two figures show that most of the grains behave as expected. That is, the plastic strain is inversely proportional to the hardness estimated from these two factors. A grain with a small Taylor factor or a large Schmid factor is expected to be soft. Therefore, it shows more plastic strain in the loading direction. The relationship is also approximately linear. Only grains with LD orientation No. 1 ([100]) are clear outliers. The explanation for these outliers needs further investigation.

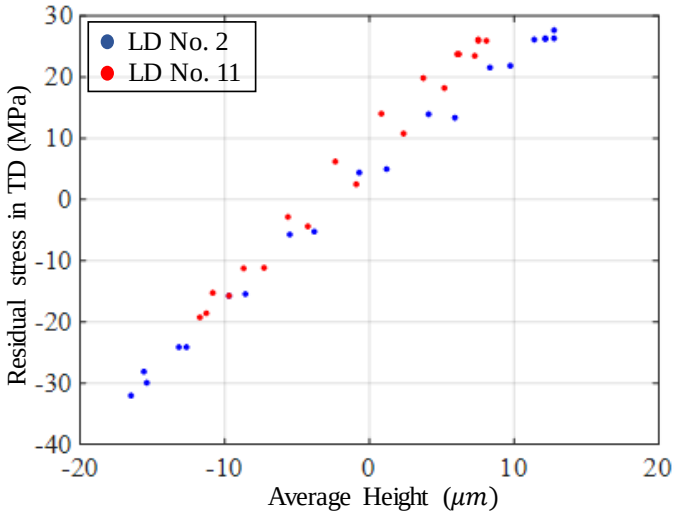

Figure 4-4. Residual stresses in the transverse direction (TD) averaged over all the grains plotted with respect to the average surface height. Results from LD orientation No. 2 & No. 11 and all NDs are shown.

While the estimate of the strains alone would be useful, we can also estimate residual stresses in TD and ND from the average height. Figure 4-4 illustrates average residual stresses in the transverse direction (TD) plotted with respect to the average surface height for grain orientations No. 2 and No. 11 and all their respective NDs. Figure 4-5 depicts average residual stresses in the normal direction (ND) plotted with respect to the average surface height for grain orientations No. 2 and No. 11 and all their respective NDs. We observed that the residual stress in TD is proportional to the average height. The residual stress in ND is inversely proportional to the average height. However, the relation is roughly linear only within grains of the same LD. As Figure 4-4 and Figure 4-5 indicate, the slopes for height and the residual stress relationship for LD grain orientations No. 2 and No. 11 are different. This difference in the slopes, when there is none in the strains, can be attributed to the anisotropic elasticity. Changes in grain orientation lead to Young's modulus or stiffness change in nickel crystals. As a result, residual stresses can only be estimated from the

surface heights if the stiffness tensor, calculated from the grain orientation, is known. However, a few qualitative predictions can still be made using just the grain-surface heights. For instance, any grain that sinks or that forms a valley (i.e., large negative height) shows compressive (negative) residual stress in the TD and tensile (positive) residual stress in the ND. Similarly, any grain that rises or that forms a peak (i.e., large positive height) shows tensile (positive) residual stress in the TD and compressive (negative) residual stress in the ND.

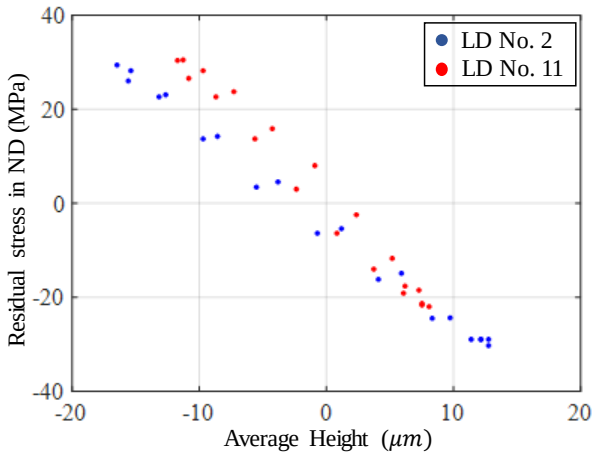

Figure 4-5. Residual stresses in the transverse direction (ND) averaged over the entire grains plotted with respect to the average surface height. Results from LD orientation No. 2 & No. 11 and all NDs are shown.

1.2. Conclusion

In the idealized simulation sample used in the previous chapter, we find that average grain height can be related to particular plastic strains. The average plastic strains in the normal and transverse directions are linearly related to the average grain-surface height. This deduction also allowed us to estimate the residual stresses from the surface height. A major conclusion is that the

strains and residual stresses in the loading direction are not related to the grain-surface heights. However, note all the plastic strains can be determined using the grain orientations.

It is important to note that we make these conclusions under the assumption that the material surrounding the grain of interest is isotropic. Under this assumption, we can use a parameter—average height relative to the average surface height—to estimate strain. However, in an actual polycrystal, measurement of this parameter might not be possible since we do not have a reference average/isotropic surface. Despite this, we believe that we can still make a qualitative assessment of residual/compressive stresses from grain sinking and rising. More importantly, we believe that this study's main contribution lies in developing a conceptual understanding of the relationship between strains in the grain and its surface height. Such understanding would allow prediction of strain localization on the surface. Further work will consider the interaction between grains of specific orientations and include validation using experimental observations.

2. The effect of neighboring grains on a grain's surface height

The analysis up to this point has revealed that the grains in the experimental polycrystal sample behave as expected only for a few specific loading direction grain orientations. Work by other researchers has predicted that the neighboring grains would play an important role in determining a grain's surface height [53], [56], [59]. Therefore, this section explores whether or not the discrepancies between experimental and single-grain simulations are the effects of the neighboring grains. In subsection 2.1, the effect of an embedded grain on the surface height of the surrounding homogenous medium. In subsection 2.2, the variation of a grain's surface height in a polycrystals is investigated.

2.1. Effect of an embedded grain on the surrounding surface height

2.1.1. Simulation setup

As in the previous chapters, we first estimated this effect of an anisotopic grain on a homogeneous isotropic medium by embedding a grain in an isotropic sample, but at multiple locations along the depth direction. Figure 4-6 illustrates some of the simulation sample configurations used in this study. It depicts the anisotropic grain in red and the isotropic medium in green. As in the previous chapters, the same columnar grain of the hexagonal cross-section was used in all configurations. The isotropic sample, however, was enlarged to a 8x8 mm cross-section and lengthened to 24 mm because we intended to study the surface heights at much farther distances away from the anisotropic grain. The enlargement was carried out based on the estimation by researchers that a grain's influence on the roughness exists for over 2–3 grain diameters [53], [74]. Five configurations were studied in total. In the first configuration (Figure 4-6 (a)), the grain lies on the surface. In the other four configurations, the grain surface lies below the sample surface at distances of 0.5, 1, 2, and 3 mm. Figure 4-6(b & c) shows grains at two different depths of 0.5 mm and 1 mm.

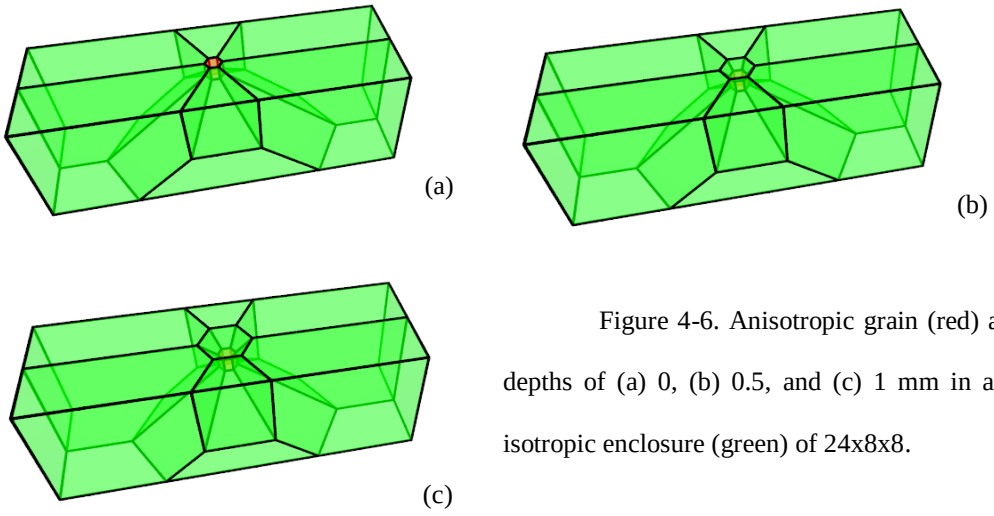

Figure 4-6. Anisotropic grain (red) at depths of (a) 0, (b) 0.5, and (c) 1 mm in an isotropic enclosure (green) of 24x8x8.

Table 4-1. Grain behavior and orientations

Grain Orientation	Behavior	Euler angles
1	Grain that rises the most	[90 135 90]
2	Grain that sinks the most	[45 90 0]
3	Grain with zero average height but peaks and valleys on the grain boundaries	[57.27 122.79 40.12]
4	Grain that sinks and shows no variation with ND	[0 0 0]

In each configuration, we used four grain orientations with distinct surface height behaviors. These surface height behaviors were determined using the single-grain simulations in the previous chapters. Table 4-1 specifies the orientations and surface height behaviors of the selected grains. Grain No.1 rises the most, No. 2 sinks the most, No. 3 has zero average height but peaks and valleys are located on the grain boundaries, and No. 4 sinks and does not exhibit any variation with ND orientation change. Also, the surface height of an entirely isotropic sample was used for reference. The crystal plasticity parameters are the same as the ones used in the previous section. The tensile loading simulation until a strain of 5% was carried out using the four selected grain orientations in each of the five sample configurations.

2.1.2. Results

From the results of each simulation, we calculation the height deviation of the sample surface from the surface height of the isotropic sample. Then, the maximum among these height deviations at all points on the sample surface from each simulation is calculated. Figure 4-7(a) illustrates the maximum deviation of the surface height from the isotropic surface using all grain orientations and grain depths. Figure 4-7(b) expresses the deviation as a percentage of the maximum deviation if the same grain lies at the surface. Note that only the magnitude of the deviation value

was used since it is expected that a rising grain will only cause the surface to rise. We are only interested in the magnitude of the influence and not its sign. First, for each grain orientation, the maximum deviation is considered. As expected the largest maximum deviation occurs when the grain is on the surface. Both the subplots indicate that the influence of the grain decreases with the depth of the grain. The influence of the subsurface grain becomes negligible (< 10% of the maximum deviation for the grain at the surface) at depths greater than three times the grain diameter (~ 1 mm). More importantly, as seen in Figure 4-7 (b), the percentage deviation behavior with respect to the depth is similar for all the grain orientations. Consequently, we could expect similar behavior from any other grain orientation as well.

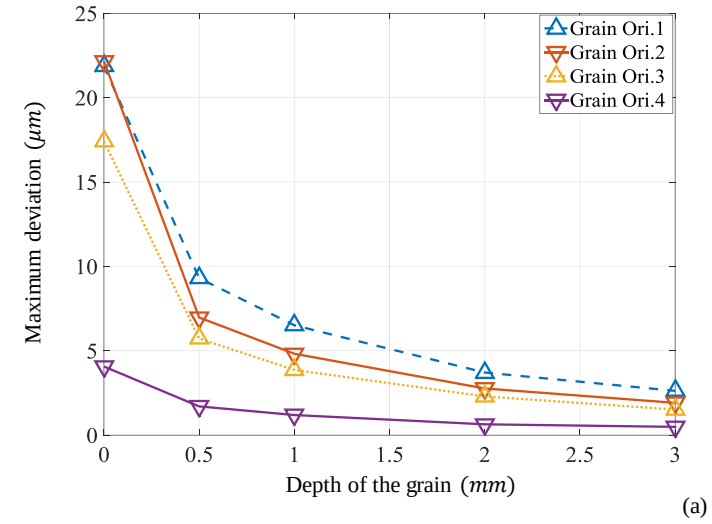

(a)

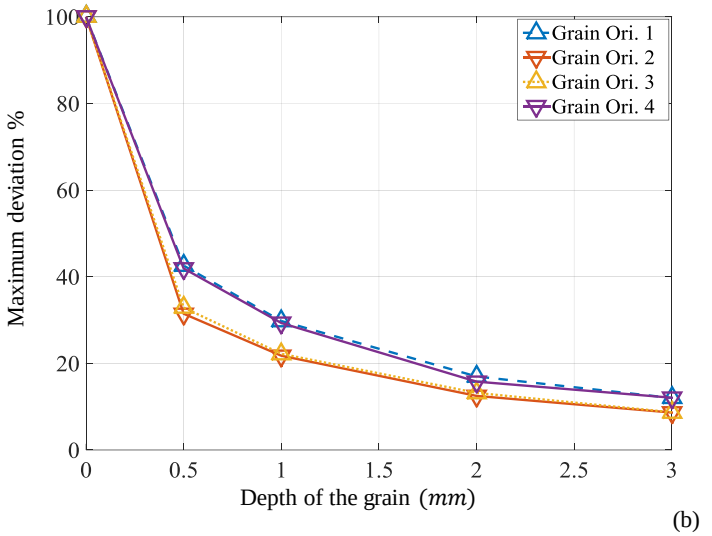

(b)

Figure 4-7. (a) The maximum deviations in the surface height from the isotropic surface; (b) the maximum deviation of the surface heights as a percentage of the maximum deviation for the same grain orientation at the surface.

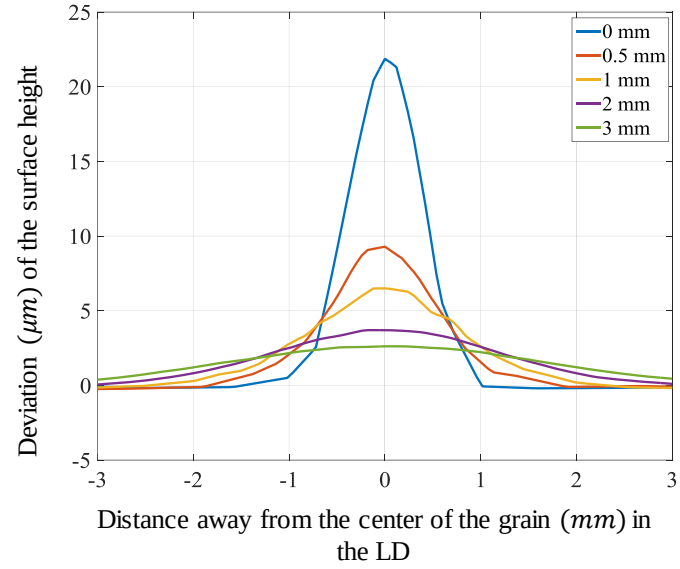

(a)

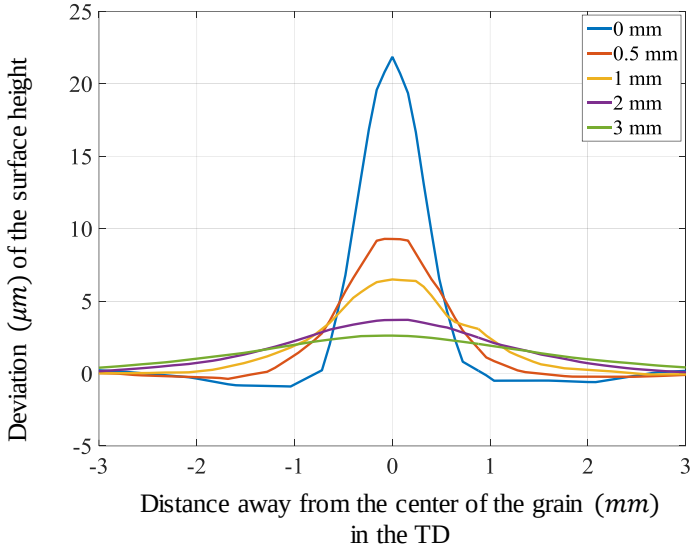

(b)

Figure 4-8. The deviation of the surface heights when using grain orientation No. 1 along the (a) LD and (b) TD.

Figure 4-8 shows the deviations of the heights at various locations of the sample surface due to the presence of grain with orientation No. 1 at different depths. Figure 4-8(a) and (b) depict

the surface-height deviations in the loading and transverse directions, respectively, for each grain depth. Zero on the x-axis of these figures represents the point on the sample surface directly above the face center of the anisotropic grains. The first observation is that the influence of an anisotropic grain is similar in both directions. The only difference is that, in the TD, when the grain lies on the surface, slight grain-surface sinking is observed near the grain boundaries even though the grain itself rises. However, we ignored this slight sinking and assumed the effect to be the same in both directions. Figure 4-8 shows that, at every grain depth, most height deviation occurs in the area directly above the embedded grain. This height deviation decreases as we consider points at greater distances away from the center of the sample. The height deviation decreases more gradually as the grain lies at greater depths. In other words, the profile peak becomes smoother at greater depths. As a result of this, for some points on the surface, a grain at a greater depth, but not lying directly underneath the point, has a larger influence on the surface height. For instance, for a point at a distance of 2 mm in the ND (Figure 4-8 (a)) from the center of the sample surface, the height deviation increases with the depth of the grain.

The most important observation is the relative influence of the position of the grain on the surface height. In Figure 4-8(a), consider the case where the grain is located on the surface. At a point on the surface, 1 mm from the center of the sample surface in the LD; the height change is almost zero. Now, consider a case where the grain lies at a depth of 1 mm from the center of the sample. The height change at the center of the sample surface is 10 μm. From this observation, we can postulate that, in a polycrystal, a subsurface grain is more influential on the grain's surface height than the in-plane neighbor located at the same distance. Similar conclusions can be made based on the results from using grains with other orientations.

From these simulations, we understand some aspects of the neighboring grains' effects on the surface height. However, it remains unclear how the grain surface behavior changes in a typical polycrystal.

2.2. Grains' surface-height change in polycrystals

2.2.1. Simulation setup

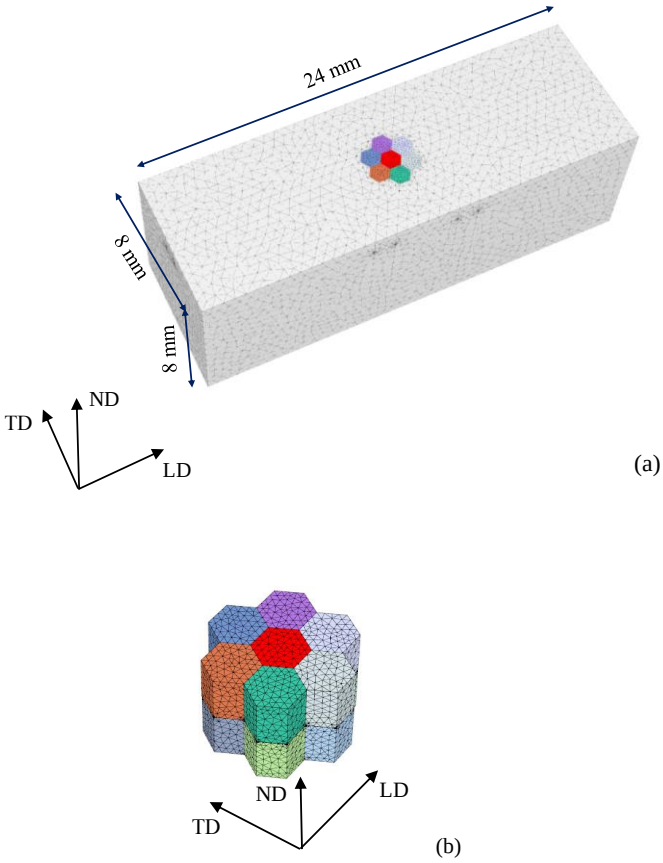

Figure 4-9 (a) The grain arrangement in the simulation sample used to investigate the effect of neighboring grains; (b) a closer look at the specific anisotropic grains in this model.

Figure 4-9 depicts the simulation sample used to estimate the effect of neighboring grains in a polycrystal. This sample resembles the one used to predict the effect of neighboring grains on the onset of plasticity by Sauzay (2006) [75]. The simulation sample consists of 14 equally sized

grains. The grains are columnar with a hexagonal face of area $0.866\ \text{mm}^2$ and a depth of 1 mm, just like the grain in the simulation sample in the previous chapters. The center grain in the top layer is the grain of interest. The rest of the grains in this sample are adjacent to the grain of interest. As we have seen in the previous section, even the non-adjacent grains—those at a distance from the grain of interest—were expected to be influential [53]. However, we ignored the non-adjacent grains because their effects were expected to be smaller.

We used nine grain orientations for the center grains. These nine grain orientations were chosen so that they would demonstrate distinct behaviors as predicted from the single-grain simulations. Figure 4-10 shows the loading-direction orientations of the first eight grains, and the 9^{th} grain is an isotropic grain. Table 4-2 specifies the orientation and the single-grain behavior of each of these center grains. Grains No. 1–3 have the same [101] loading-direction orientation. Grain No. 1 rises the most, and grain No. 2 sinks the most among all grain orientations. Grains No. 4–6 have the same LD orientation close to the center of the IPF. Grains No. 4 and 6 rise and sink but less than the grains with [101] LD orientation. Grains 7 and 8 lie at the other two vertices of the LD IPF. Figure 4-11 illustrates the average surface heights of the selected center-grain orientations obtained from single-grain simulations in Chapter 3, section 4.2. For each specific center grain, 40 sets of random orientations were used for 13 neighboring grains. Sauzay (2006) [75] determined 40 sets of random orientation to represent all kinds of grain orientation combinations when using FCC crystals. In total, 360 grain arrangements have been simulated. The crystal plasticity parameters are the same as the ones used in the previous two chapters. The sample was stretched to an axial strain of 1%.

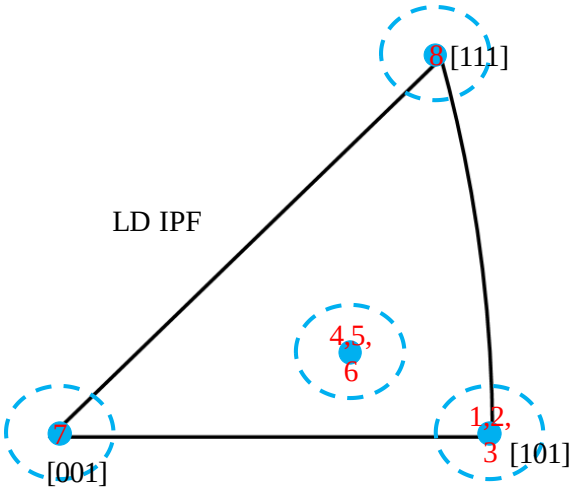

Figure 4-10. Loading-direction orientations of the eight different center grains used.

Table 4-2. Center-grain behavior and orientation

Center Grain No.	Behavior	Euler angles
1	rises the most	90, 135, 90
2	sinks the most	45, 90, 0
3	zero average height but peaks and valleys on the grain boundaries	57.27, 122.79, 40.12
4	rises less than No.1	-87.24, 124.49, 78
5	sinks less than No. 2	67.94, 117.34, 31.78
6	zero average height	79.24, 123.07, 53.95
7	sinks and shows no variation with ND	0, 0,0
8	sinks slightly and shows no variation with change in ND	-54.73, 135,90
9	isotropic	-

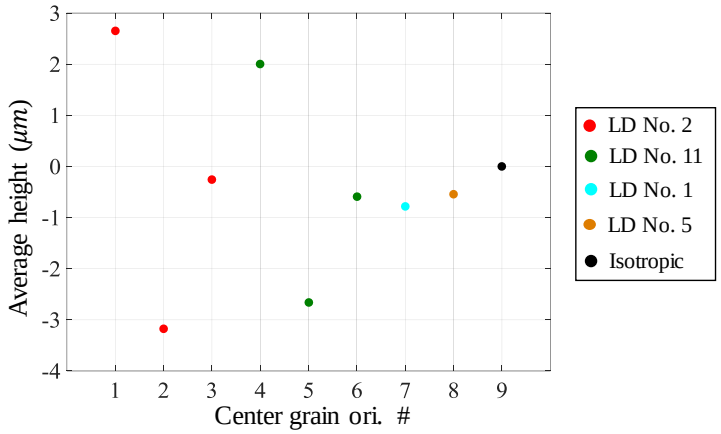

Figure 4-11. Average surface heights obtained from single-grain simulations of the selected center-grain orientations.

2.2.2. Results

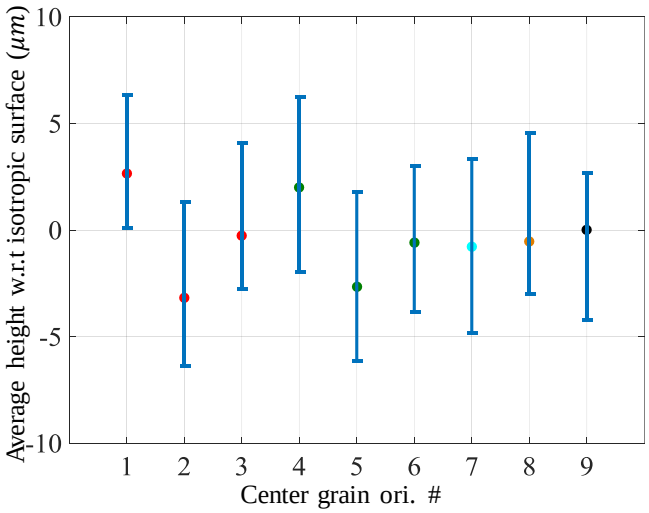

Figure 4-12. Average grain-surface heights of all grains arrangements at an axial deformation of 1%. Vertical bars denote the range of height variations arising from different neighboring grains sets for the same center grain. Markers indicate heights from single grain simulations.

Figure 4-12 illustrates the average height of the center grain with reference to an isotropic sample from all 360 simulations. Center grain numbers are listed on the x-axis. The vertical bars in the figure denote the range of height variations resulting from the change of the neighboring grains. These results indicate that almost all grains can rise or sink depending on the neighboring grains. Only grain No. 1, which is expected to rise the most in single-grain simulations, rose in all cases. However, there are cases where the grain surface rises only a little relative to the isotropic surface. Considering all the center grains, height variations from the neighboring grains are always very large. These height variations are as large as the as the largest height change from the change in orientation of the center grain itself.

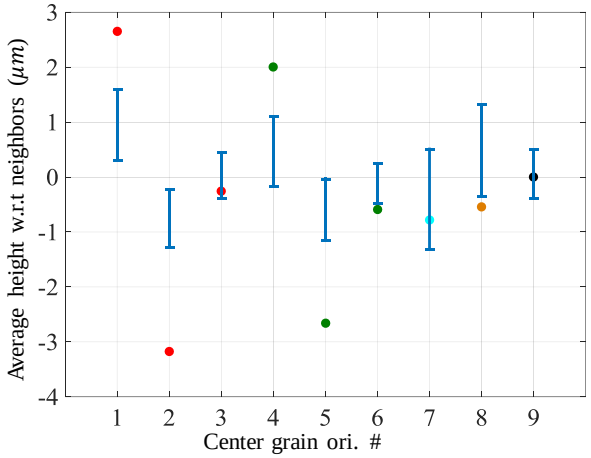

Figure 4-13. Average grain-surface heights relative to the neighboring grains. Vertical bars denote the range of height variations arising from different neighboring grains sets for the same center grain. Markers indicate heights from single-grain simulations.

In the experimental analysis, we determined grain surface rising/sinking behavior by calculating the average surface height relative to the neighboring grains as opposed to the entire

gauge area. Therefore, we followed the same procedure to analyze these simulation results as well. Figure 4-13 is similar to Figure 4-12 in all aspects, except that the average height was calculated with respect to the average surface height of the six in-plane neighboring grains. The average height of the neighboring grains varied in each of the 360 simulations and was not constant. By using such a calculation of height, the height variations resulting from the neighboring grains were much smaller (see Figure 4-13). As a result, grains No. 1, 2, 4, and 5 behaved just as predicted in the single-grain simulations. This observation indicates that using the grain height relative to the height of the neighborhood results in a better match to the surface behavior prediction obtained considering only the orientation of the grain itself. Grain No. 7, positioned near [100] LD orientation, still mostly sank irrespective of neighboring grains, as observed in the experimental results in Chapter 3. Similarly, Grain No. 8, positioned near [111] LD orientation, was observed to sink in the simulations, and it also sinks most of the time according to the experimental observations in Chapter 3. However, under the influence of the neighboring grains, it rose most of the times, as seen in Figure 4-13. The reason for this observation is not yet clear and it is left for the future work. The grains No. 1, 2, 4, and 5 in Figure 4-13 are the grains that were expected to rise and sink more than the grains with other orientations. Therefore, we can conclude that surface behavior prediction from the grain orientation can only be carried out for the grains that are expected to sink or rise the most. These grains that can both sink and rise the most lie near the LD IPF vertex [101]. Next, we analyzed the surface of the experimental sample to verify if the grain orientations that were expected to rise and sink the most behave in the same way.

2.2.3. Experimental observations

From the single-grain simulations in Chapter 3, we calculated simulated average surface heights for all the grain orientations identified in the experimental sample. Using this data, we chose grains whose heights differed from the isotropic surface (zero height) by a large value. This value is three times the standard deviations of all the simulated heights. Figure 4-14 illustrates the LD orientations of the five grains identified in such a way. As expected, all these grains have LD orientations close to the IPF vertex [101].

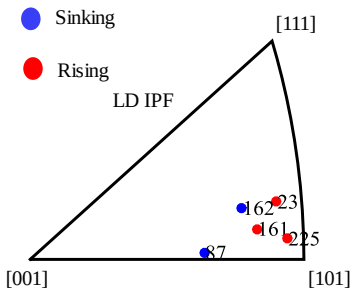

Figure 4-14. Loading direction IPF showing the grains expected to rise and sink the most.

Figure 4-15 depicts the measured surface heights of the sample deformed in the experiments. The same grains in Figure 4-14 are also identified here and are labeled using the same numbering order. Figure 4-15 (a) also specifies the average height (in μm) of the five identified grains relative to their neighborhood and labels them. This average height indicates grain-surface sinking and rising. Comparing these observed grain surface sinking to the expected grain surface behavior in Figure 4-14, four of the five grain surfaces behave as expected. Only grain No. 225 sank when expected to rise. When we disregarded the smallest grains, all the three remaining grains behaved as predicted by single-grain simulation (Figure 4-15(b)). This demonstrates that predictions

of single simulations are true but often not observed in the experiments only because of neighboring grains.

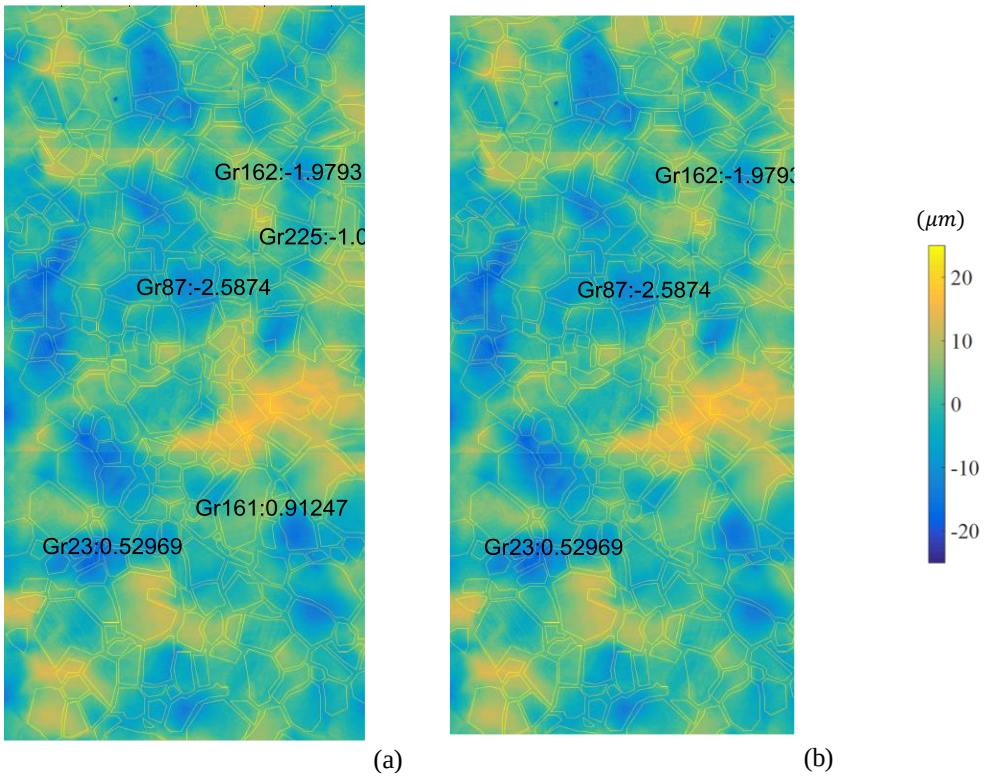

Figure 4-15. Surface heights of the gage area. The identified grains are numbered, and their average height relative to their neighborhood in μm is shown. (a) All identified grains; (b) smallest grains are disregarded.

2.3. Conclusion

We can conclude that the neighboring grains, especially the grains lying underneath the surface up to depths of 3–4 times the grain diameter, influence the surface height. In comparison, the effect of the in-plane neighboring grains is lesser. Because of these results, we expect that the consideration of subsurface grains would be necessary for the accurate prediction of surface heights. In addition, in typical polycrystals, neighboring grains are highly influential in determining the grain-surface heights and often dominate the surface behavior of the grain itself when the surface behavior is determined using the height of the isotropic material as the reference. However, the neighboring grains are slightly less influential on the grain-surface behavior when the average height of the neighboring grains is used as the reference. In this case, the grains that were expected to rise or sink the most behaved in the same way irrespective of the neighboring grains. Only for such grains does the orientation of the grain dictate its surface behavior.

Chapter 5

CONCLUSIONS AND FUTURE WORK

This research work investigated several aspects of surface roughness formation in nickel polycrystals during small amounts of tensile plastic loading. It relates surface-roughness features, both at the level of slip steps and grains, to their stress and strain distributions using simulations. To determine the stresses and elastic strains associated with slip steps (i.e., the dislocation intersection with the surface), this work developed a novel numerical approach, which has achieved large savings in computational time when compared to traditional numerical approaches. Based on this, a journal paper entitled "A Combined Dislocation Fan-Finite Element (DF-FE) Method for Stress Field Simulation of Dislocations Emerging at the Free Surfaces of 3D Elastically Anisotropic Crystals" was published and presented as Chapter 2 in this dissertation [76]. This study also carried out some preliminary work in determining the relationship between average grain-surface height and average grain strains and stresses for all grain orientations using crystal plasticity finite element simulations. We established that a grain's average plastic strain in the loading direction is not related to its surface height. However, strains and stresses in the other two directions are linearly proportional to the surface height. In the same process, a qualitative relationship between grain heights and residual stresses was found. Based on this grain-scale work, a conference paper titled "A CPFEM Investigation of the Effect of Grain Orientation on the Surface Profile During Tensile Plastic Deformation of FCC Polycrystals" was presented and published in the proceedings [77]. The validation of these stress and strain distributions using experimental observations remains a task left for future work.

This research work led to an understanding of the relationship between surface roughness formation and the surface-grain orientations using both experimental observations and simulations.

In experiments, a surface white light interferometer (SWLI) measured surface heights, and electron backscatter diffraction (EBSD) characterized grain orientations on the surface. Simulations were carried out using the crystal plasticity finite element method (CPFEM). This work first disproved an assumption that a grain's hardness, as estimated by Schmid or Taylor factors, determines the grain surface height. Additionally, this work establishes that the grain orientation in the loading direction does not uniquely determine the grain-surface height. It is the grain's deformation in the normal direction, for a specific loading direction orientation, that determines the grain-surface height. Based on this work relating the grain orientation and surface height, a manuscript entitled "Investigating the Relationship Between Grain Orientation and Surface Height Changes in Nickel Polycrystals Under Tensile Plastic Deformation" was submitted for journal publication and presented as Chapter 3 in this dissertation.

The results until now utilized simulations considering only the orientation of the grain itself ignoring the neighboring grains in a polycrystal. That is why, these results can be termed as the predicted surface height behavior of a grain resulting from its orientation. However, experiments showed that, for many grain orientations, a grain's surface does not always behave as predicted. This research work contains some preliminary results that demonstrated that the effect of the neighboring grains causes these discrepancies. Neighboring grains, both the in-plane and the subsurface grains, substantially modify a grain's surface height. Moreover, among the neighboring grains, the grain directly underneath (subsurface grain) has the most influence. Subsurface grains even up to a depth of 3–4 grain diameters have been found to be influential. Despite the substantial influence of the neighboring grains, there are grains of specific orientations whose predicted surface behavior is consistently observed in experimental observations. Grains with the loading direction orientations near [101], i.e., those that are predicted to have the highest or the lowest surface heights, behave as predicted. Apart from these, the grains that have loading direction orientations near [100] and [111] also behave as predicted.

This study also found a gap of scales between slip-step simulations using discrete dislocations and experimental validation using SWLI. Even though simulation efficiency improved using our proposed numerical method, discrete dislocation simulation is still very computationally expensive. That is why the samples sizes are still limited to a maximum of a few micrometers. Moreover, individual slip steps are only separated by a few nanometers. SWLI has a maximum spatial resolution of only around 0.4 μm; as a result, individual slip steps cannot be resolved by SWLI. Helpfully, under tensile loading, grain-scale roughening dominates surface height and not slip steps. This justified the focus on grain-scale roughness in this dissertation.

This study's conclusions have implications for future research work concerning roughness at both slip-step scale and grain scale. The gap between scales implies that study of slip steps in polycrystals requires bridging of the scales from the viewpoint of both simulations and experimental capabilities. The scale of the simulations could be increased using additional computational power and efficient modeling. An alternative approach would be to use statistical modeling of dislocations instead of explicit treatment. Doing so, the scale of simulations could be increased. Experimental capabilities, both testing, and profiling, at a microscale are required. In studies considering grain-scale roughening, complete and quantitative prediction of grain-surface behavior requires consideration of the morphology and orientation of grains underneath the surface up to a depth of few grain diameters. Additionally, experimental validation of CPFEM simulations in this study confirms the utility of the phenomenological crystal plasticity models and their implementation using finite elements in simulating features of grain-scale plasticity.

The conclusions of the study have implications for the investigation of grain orientation influence on failure through the growth of voids on the surface of the sample under tensile loading. Based on the preliminary results, the simulation can predict tensile residual stresses in the in-plane direction normal to the loading axis based on a grain's orientation as well as its rising grain surface. The stresses in the direction normal to the surface are always zero on the surface. As a result, a

grains surface that rises would lead to tensile hydrostatic stresses (i.e., the sum of the normal stresses in all three directions). Since large tensile hydrostatic stresses are favorable to void growth [78], this study predicts that a rising grain favors void growth. Using the same explanation, void growth could be less favorable on a grain surface that sinks. This study also has implications on the investigation of the role of grain orientation in growth cracks. Grain orientation is known to be highly influential on the growth of small cracks [79]. This research work relates the residual stresses in surface grains to their orientations. Since the residual stresses, among other factors, are known to influence crack growth, this study can be potentially extended to relate crack growth and grain orientation.

Since we only considered the surface grain in this study, the findings are more applicable to loading cases where the stress at the surface is the largest. One such loading is bending. In bending, the most intense stresses occur on the surface. The subsurface grains would be under smaller loads and thereby undergo a smaller amount of plastic strain. Therefore, it can be expected that the relation between grain orientation and its surface height determined in this study would be clearly observed [80]. Currently, in bending, there is only an understanding of the relationship between surface roughness statistics and grain orientation distributions and not between specific grain orientations and grain surface height[62].

More importantly, in bending, failure is known to initiate on the stretched surface through the formation of shear bands [81]–[83]. It is also known that the failure strength depends on the surface-grain orientation distribution [81]. However, the relationship between individual grain orientations to the strain localization (shear band formation on the surface) and failure has not been established. The investigation of this relationship could benefit from our conclusions on grain surface height, deformation fields, and grain orientation.

In the light of the conclusions from our study, there are several logical extensions of this work. First, strains and stresses in surface grains have to be measured to validate their relationship to grain orientations and surface heights. One such method that can carry out high-resolution strain

measurements at fine spatial resolutions is high-resolution EBSD [84]. Another immediate future task is to consider the contribution of the neighboring grain on the surface roughness, which can be done by characterizing the grains underneath the surface. Most of the currently available methods that characterize the orientations of the subsurface grains involve sectioning the grains [85], [86], and thus are destructive. For this reason, characterizing the subsurface grains is only possible after mechanical testing which can be a potential limitation. An alternative to destructive testing is to minimize the influence of the subsurface grains using the bending tests mentioned previously.

REFERENCES

[1] S. D. Antolovich and R. W. Armstrong, "Plastic strain localization in metals: Origins and consequences," *Prog. Mater. Sci.*, vol. 54, no. March 2013, pp. 1–160, 2014.

[2] Y. Wang, E. I. Meletis, and H. Huang, "Quantitative study of surface roughness evolution during low-cycle fatigue of 316L stainless steel using Scanning Whitelight Interferometric (SWLI) Microscopy," *Int. J. Fatigue*, vol. 48, pp. 280–288, 2013.

[3] R. Kelton, J. Fathi, E. I. Meletis, and H. Huang, "Study of the Surface Roughness Evolution of Pinned Fatigue Cracks, and its Relation to Crack Pinning Duration and Crack Propagation Rate Between Pinning Points," in *Volume 9: Mechanics of Solids, Structures and Fluids; NDE, Structural Health Monitoring and Prognosis*, 2017, p. V009T12A007.

[4] R. Kelton, J. F. Sola, E. I. Meletis, and H. Huang, "Visualization and Quantitative Analysis of Crack-Tip Plastic Zone in Pure Nickel," *Jom*, vol. 70, no. 7, pp. 1175–1181, 2018.

[5] R. LeSar, "Simulations of Dislocation Structure and Response," *Annu. Rev. Condens. Matter Phys.*, vol. 5, no. 1, pp. 375–407, 2014.

[6] R. Pokharel, J. Lind, A. K. Kanjarla, R. A. Lebensohn, S. F. Li, P. Kenesei, R. M. Suter, and A. D. Rollett, "Polycrystal Plasticity: Comparison Between Grain - Scale Observations of Deformation and Simulations," *Annu. Rev. Condens. Matter Phys.*, vol. 5, no. 1, pp. 317–346, Mar. 2014.

[7] A. D. Rollett, G. S. Rohrer, and R. M. Suter, "Understanding materials microstructure and behavior at the mesoscale," *MRS Bull.*, vol. 40, no. 11, pp. 951–958, 2015.

[8] F. Roters, P. Eisenlohr, L. Hantcherli, D. D. Tjahjanto, T. R. Bieler, and D. Raabe, "Overview of constitutive laws, kinematics, homogenization and multiscale methods in crystal plasticity finite-element modeling: Theory, experiments, applications," *Acta Mater.*, vol. 58, no. 4, pp. 1152–1211, 2010.

[9] A. Alankar, "Development of a 3D Microstructure Sensitive Crystal Plasticity Model for Aluminum," 2010.

[10] A. M. Hussein, S. I. Rao, M. D. Uchic, D. M. Dimiduk, and J. A. El-Awady, "Microstructurally based cross-slip mechanisms and their effects on dislocation microstructure evolution in fcc crystals," *Acta Mater.*, vol. 85, pp. 180–190, 2015.

[11] J. A. El-Awady, "Unravelling the physics of size-dependent dislocation-mediated plasticity.," *Nat. Commun.*, vol. 6, no. May 2014, p. 5926, 2015.

[12] H. Tang, K. W. Schwarz, and H. D. Espinosa, "Dislocation escape-related size effects in single-crystal micropillars under uniaxial compression," *Acta Mater.*, vol. 55, no. 5, pp. 1607–1616, 2007.

[13] C. Zhou and R. Lesar, "Dislocation dynamics simulations of plasticity in polycrystalline thin films," *Int. J. Plast.*, vol. 30–31, pp. 185–201, 2012.

[14] H.-J. Chang, M. Fivel, D. Rodney, and M. Verdier, "Multiscale modelling of indentation in FCC metals: From atomic to continuum," *Comptes Rendus Phys.*, vol. 11, no. 3–4, pp. 285–292, 2010.

[15] G. Po, M. S. Mohamed, T. Crosby, C. Erel, A. El-Azab, and N. Ghoniem, "Recent Progress in Discrete Dislocation Dynamics and Its Applications to Micro Plasticity," *Jom*, vol. 66, no. 10, pp. 2108–2120, 2014.

[16] S. Groh and H. M. Zbib, "Advances in Discrete Dislocations Dynamics and Multiscale Modeling," *J. Eng. Mater. Technol.*, vol. 131, no. 4, p. 041209, 2009.

[17] J. P. Hirth and J. Lothe, *Theory of Dislocations*. Krieger Publishing Company, 1982.

[18] D. J. Bacon and D. M. Barnett, "Anisotropic continuum theory of lattice defects," vol. 23, no. X, 1979.

[19] P. P. Groves and D. J. Bacon, "The dislocation loop near a free surface," *Philos. Mag.*, vol.

22, no. 175, pp. 83–91, 1970.
[20] Y. Maurissen and L. Capella, “Stress field of a dislocation segment parallel to a free surface,” *Philos. Mag.*, 1974.
[21] Y. Maurissen and L. Capella, “Stress field of a dislocation segment perpendicular to a free surface,” *Philos. Mag.*, 1974.
[22] E. H. Yoffe, “A dislocation at a free surface,” *Philosophical Magazine*, vol. 6, no. 69. pp. 1147–1155, 1961.
[23] M. Comninou and J. Dundurs, “The angular dislocation in a half space,” *J. Elast.*, vol. 5, no. 3–4, pp. 203–216, 1975.
[24] K. Honda, “Dislocation Walls Consisting of Double Arrays in White Tin Single Crystals,” *Jpn. J. Appl. Phys.*, vol. 18, no. 2, pp. 215–224, 1979.
[25] T. J. Gosling and J. R. Willis, “A line-integral representation for the stresses due to an arbitrary dislocation in an isotropic half-space,” *J. Mech. Phys. Solids*, vol. 42, no. 8, pp. 1199–1221, 1994.
[26] E. Van der Giessen and A. Needleman, “Discrete dislocation plasticity: a simple planar model,” *Model. Simul. …*, 1995.
[27] D. Weygand, L. H. Friedman, E. Van Der Giessen, and a Needleman, “Aspects of boundary-value problem solutions with three-dimensional dislocation dynamics,” *Model. Simul. Mater. Sci. Eng.*, vol. 10, no. 4, pp. 437–468, 2002.
[28] H. M. Zbib and T. Diaz de la Rubia, “A multiscale model of plasticity,” *Int. J. Plast.*, vol. 18, pp. 1133–1163, 2002.
[29] R. Martinez and N. M. Ghoniem, “The influence of crystal surfaces on dislocation interactions in mesoscopic plasticity: A combined dislocation dynamics-finite element approach,” *C. - Comput. Model. Eng. Sci.*, vol. 3, no. 2, pp. 229–243, 2002.
[30] a Arsenlis, W. Cai, M. Tang, M. Rhee, T. Oppelstrup, G. Hommes, T. G. Pierce, and V. V Bulatov, “Enabling strain hardening simulations with dislocation dynamics,” *Model. Simul. Mater. Sci. Eng.*, vol. 15, no. 6, pp. 553–595, 2007.
[31] J. a. El-Awady, S. Bulent Biner, and N. M. Ghoniem, “A self-consistent boundary element, parametric dislocation dynamics formulation of plastic flow in finite volumes,” *J. Mech. Phys. Solids*, vol. 56, no. 5, pp. 2019–2035, 2008.
[32] M. C. Fivel, T. J. Gosling, and G. R. Canova, “Implementing image stresses in a 3D dislocation simulation,” *Model. Simul. Mater. Sci. Eng.*, vol. 4, no. 6, pp. 581–596, 1999.
[33] T. a. Khraishi and H. M. Zbib, “Free-Surface Effects in 3D Dislocation Dynamics: Formulation and Modeling,” *J. Eng. Mater. Technol.*, vol. 124, no. 3, p. 342, 2002.
[34] X. H. Liu and K. W. Schwarz, “Modelling of dislocations intersecting a free surface,” *Model. Simul. Mater. Sci. Eng.*, vol. 13, no. 8, pp. 1233–1247, 2005.
[35] M. Tang, G. Xu, W. Cai, and V. Bulatov, “Dislocation Image Stresses at Free Surfaces by the Finite Element Method,” *MRS Proc.*, vol. 795, p. U2.4, 2003.
[36] M. Tang, W. Cai, G. Xu, and V. V Bulatov, “A hybrid method for computing forces on curved dislocations intersecting free surfaces in three-dimensional dislocation dynamics,” *Model. Simul. Mater. Sci. Eng.*, vol. 14, no. 7, pp. 1139–1151, 2006.
[37] M. Rhee, J. S. Stolken, V. V. Bulatov, T. D. De La Rubia, H. M. Zbib, and J. P. Hirth, “Dislocation stress fields for dynamic codes using anisotropic elasticity: Methodology and analysis,” *Mater. Sci. Eng. A*, vol. 309–310, pp. 288–293, 2001.
[38] S. Groh, B. Devincre, and L. Kubin, “Dislocations and elastic anisotropy in heteroepitaxial metallic thin films,” *Philos. …*, 2003.
[39] X. Han, N. M. Ghoniem†, and Z. Wang, “Parametric dislocation dynamics of anisotropic crystals,” *Philos. Mag.*, vol. 83, no. 31–34, pp. 3705–3721, 2003.
[40] S. P. Fitzgerald, S. Aubry, S. L. Dudarev, and W. Cai, “Dislocation dynamics simulation of Frank-Read sources in anisotropic α-Fe,” *Model. Simul. Mater. Sci. Eng.*, vol. 20, no. 4, p.

045022, 2012.
[41] S. . Fitzgerald and S. . Dudarev, "Dislocation pile-ups in Fe at high temperature," *Proc. R. Soc. A Math. Phys. Eng. Sci.*, vol. 464, no. 2098, pp. 2549–2559, Oct. 2008.
[42] S. Aubry, S. P. Fitzgerald, S. L. Dudarev, and W. Cai, "Equilibrium shape of dislocation shear loops in anisotropic α-Fe," *Model. Simul. Mater. Sci. Eng.*, vol. 19, no. 6, p. 065006, 2011.
[43] J. Yin, D. M. Barnett, and W. Cai, "Efficient computation of forces on dislocation segments in anisotropic elasticity," *Model. Simul. Mater. Sci. Eng.*, vol. 18, no. 4, p. 045013, 2010.
[44] J. Lothe, V. L. Indenbom, and V. A. Chamrov, "Elastic field and self-force of dislocations emerging at the free surfaces of an anisotropic halfspace," *Phys. status solidi*, vol. 111, no. 2, pp. 671–677, 1982.
[45] M. P. O'Day and W. a. Curtin, "A Superposition Framework for Discrete Dislocation Plasticity," *J. Appl. Mech.*, vol. 71, no. 6, pp. 805–815, 2004.
[46] J. Eshelby and A. Stroh, "Dislocations in thin plates," *Philos. Mag.*, no. March 2014, pp. 37–41, 1951.
[47] H. M. Ledbetter and E. R. Naimon, "Elastic properties of metals and alloys, I. Iron, Nickel, and Iron-Nickel Alloys," *J. Phys. Chem. Ref. Data*, vol. 2, no. 3, pp. 531–617, 1973.
[48] S. Aubry and A. Arsenlis, "Use of spherical harmonics for dislocation dynamics in anisotropic elastic media," *Model. Simul. Mater. Sci. Eng.*, vol. 21, no. 6, p. 065013, Sep. 2013.
[49] J. Yin, D. M. Barnett, S. P. Fitzgerald, and W. Cai, "Computing dislocation stress fields in anisotropic elastic media using fast multipole expansions," *Model. Simul. Mater. Sci. Eng.*, vol. 20, no. 4, p. 045015, 2012.
[50] B. Liu, A. Arsenlis, and S. Aubry, "Computing forces on interface elements exerted by dislocations in an elastically anisotropic crystalline material," *Model. Simul. Mater. Sci. Eng.*, vol. 24, no. 5, p. 055013, Jan. 2016.
[51] V. Indenbom and V. Alshits, "Dislocations in Anisotropic Media and Radon's Transformation," *Phys. status solidi*, 1974.
[52] P. D. Wu, D. J. Lloyd, M. Jain, K. W. Neale, and Y. Huang, "Effects of spatial grain orientation distribution and initial surface topography on sheet metal necking," *Int. J. Plast.*, vol. 23, no. 6, pp. 1084–1104, 2007.
[53] R. Becker, "Effects of strain localization on surface roughening during sheet forming," *Acta Mater.*, vol. 46, no. 4, pp. 1385–1401, 1998.
[54] D. Raabe, M. Sachtleber, H. Weiland, G. Scheele, and Z. Zhao, "Grain-scale micromechanics of polycrystal surfaces during plastic straining," *Acta Mater.*, vol. 51, no. 6, pp. 1539–1560, 2003.
[55] P. S. Lee, H. R. Piehler, B. L. Adams, G. Jarvis, H. Hampel, and A. D. Rollett, "Influence of surface texture on orange peel in aluminum," *J. Mater. Process. Technol.*, vol. 80–81, no. 0, pp. 315–319, 1998.
[56] Y. S. Choi, H. R. Piehler, and a. D. Rollett, "Formation of mesoscale roughening in 6022-T4 Al sheets deformed in plane-strain tension," *Metall. Mater. Trans. A*, vol. 35, no. 2, pp. 513–524, 2004.
[57] O. Wouters, W. P. Vellinga, R. van Tijum, and J. T. M. De Hosson, "Effects of crystal structure and grain orientation on the roughness of deformed polycrystalline metals," *Acta Mater.*, vol. 54, no. 10, pp. 2813–2821, 2006.
[58] M. Sauzay, "Cubic elasticity and stress distribution at the free surface of polycrystals," *Acta Mater.*, vol. 55, no. 4, pp. 1193–1202.
[59] M. R. Stoudt, L. E. Levine, A. Creuziger, and J. B. Hubbard, "The fundamental relationships between grain orientation, deformation-induced surface roughness and strain localization in an aluminum alloy," *Mater. Sci. Eng. A*, vol. 530, no. 1, pp. 107–116, 2011.

[60] Z. Zhao, R. Radovitzky, and a. Cuitiño, "A study of surface roughening in fee metals using direct numerical simulation," *Acta Mater.*, vol. 52, pp. 5791–5804, 2004.
[61] J. Rossiter, a. Brahme, K. Inal, and R. Mishra, "Numerical analyses of surface roughness during bending of FCC single crystals and polycrystals," *Int. J. Plast.*, vol. 46, pp. 82–93, 2013.
[62] W. Muhammad, U. Ali, A. P. Brahme, J. Kang, R. K. Mishra, and K. Inal, "Experimental analyses and numerical modeling of texture evolution and the development of surface roughness during bending of an extruded aluminum alloy using a multiscale modeling framework," *Int. J. Plast.*, pp. 1–29, 2017.
[63] C. H. Pham, S. Thuillier, and P. Y. Manach, "Prediction of flow stress and surface roughness of stainless steel sheets considering an inhomogeneous microstructure," *Mater. Sci. Eng. A*, vol. 678, no. September, pp. 377–388, 2016.
[64] Z. Zhao, M. Ramesh, D. Raabe, A. M. Cuitiño, and R. Radovitzky, "Investigation of three-dimensional aspects of grain-scale plastic surface deformation of an aluminum oligocrystal," *Int. J. Plast.*, vol. 24, no. 12, pp. 2278–2297, 2008.
[65] S. Ha, J.-H. Jang, and K. Kim, "Finite element implementation of dislocation-density-based crystal plasticity model and its application to pure aluminum crystalline materials," *Int. J. Mech. Sci.*, vol. 120, no. December 2016, pp. 249–262, 2016.
[66] R. Quey, P. R. Dawson, and F. Barbe, "Large-scale 3D random polycrystals for the finite element method: Generation, meshing and remeshing," *Comput. Methods Appl. Mech. Eng.*, vol. 200, no. 17–20, pp. 1729–1745, 2011.
[67] F. Roters, P. Eisenlohr, C. Kords, D. D. Tjahjanto, M. Diehl, and D. Raabe, "DAMASK: The dusseldorf advanced material simulation kit for studying crystal plasticity using an fe based or a spectral numerical solver," *Procedia IUTAM*, vol. 3, pp. 3–10, 2012.
[68] T. J. Turner, P. a Shade, J. C. Schuren, and M. a Groeber, "The influence of microstructure on surface strain distributions in a nickel micro-tension specimen," *Model. Simul. Mater. Sci. Eng.*, vol. 21, no. 1, p. 015002, 2013.
[69] D. Peirce, R. J. Asaro, and A. Needleman, "Material rate dependence and localised deformation in crystalline solids," *Acta Metall.*, vol. 31, no. 12, pp. 1951–1976, 1983.
[70] W. F. Hosford, *Mechanical behavior of materials*. Cambridge University Press, 2005.
[71] S. R. Kalidindi and L. Anand, "Large deformation simple compression of a copper single crystal," *Metall. Trans. A*, vol. 24, no. 4, pp. 989–992, 1993.
[72] A. J. Beaudoin, J. D. Bryant, and D. A. Korzekwa, "Analysis of ridging in aluminum auto body sheet metal," *Metall. Mater. Trans. a-Physical Metall. Mater. Sci.*, vol. 29, no. 9, pp. 2323–2332, 1998.
[73] S. R. Kalidindi and L. Anand, "An approximate procedure for predicting the evolution of crystallographic texture in bulk deformation processing of fcc metals," *Int. J. Mech. Sci.*, vol. 34, no. 4, pp. 309–329, 1992.
[74] A. Valkonen, *Plastic deformation and roughness of free metal surfaces*. Teknillinen korkeakoulu, 1988.
[75] M. Sauzay, "Cubic elasticity and stress distribution at the free surface of polycrystals," *Acta Mater.*, vol. 55, no. 4, pp. 1193–1202, 2007.
[76] K. Balusu and H. Huang, "A combined dislocation fan-finite element (DF-FE) method for stress field simulation of dislocations emerging at the free surfaces of 3D elastically anisotropic crystals," *Model. Simul. Mater. Sci. Eng.*, vol. 25, no. 3, p. 0355007 (14pp), 2017.
[77] K. Balusu and H. Huang, "A CPFEM Investigation of the Effect of Grain Orientation on the Surface Profile During Tensile Plastic Deformation of FCC polycrystals," *ASME Int. Mech. Eng. Congr. Expo. Proc.*, vol. 9, pp. 1–6, 2017.
[78] W. F. Hosford and R. M. Caddell, *Metal forming: Mechanics and metallurgy*. 2011.

[79] S. Kumar and W. A. Curtin, “Crack interaction with microstructure,” *Materials Today*, vol. 10, no. 9. pp. 34–44, 2007.

[80] Y. Shi, P. Z. Zhao, H. Jin, P. D. Wu, and D. J. Lloyd, “Analysis of Surface Roughening in AA6111 Automotive Sheet Under Pure Bending,” *Metall. Mater. Trans. A Phys. Metall. Mater. Sci.*, vol. 47, no. 2, pp. 949–960, 2016.

[81] M. Dao and M. Lit, “A micromechanics study on strain-localization-induced fracture initiation in bending using crystal plasticity models,” *Philos. Mag. A Phys. Condens. Matter, Struct. Defects Mech. Prop.*, vol. 81, no. 8, pp. 1997–2020, 2001.

[82] J. Sarkar, T. R. G. Kutty, K. T. Conlon, D. S. Wilkinson, J. D. Embury, and D. J. Lloyd, “Tensile and bending properties of AA5754 aluminum alloys,” 2001.

[83] C. Soyarslan, M. Malekipour Gharbi, and A. E. Tekkaya, “A combined experimental-numerical investigation of ductile fracture in bending of a class of ferritic-martensitic steel,” *Int. J. Solids Struct.*, vol. 49, no. 13, pp. 1608–1626, 2012.

[84] A. J. Wilkinson, T. B. Britton, J. Jiang, and P. S. Karamched, “A review of advances and challenges in EBSD strain mapping,” *IOP Conf. Ser. Mater. Sci. Eng.*, vol. 55, p. 012020, 2014.

[85] H. Jin, P. D. Wu, M. D. Ball, and D. J. Lloyd, “Three-dimensional texture determination of 6111 aluminium alloy sheet by precise serial sectioning and EBSD measurement,” *Mater. Sci. Technol.*, vol. 21, no. 4, pp. 419–428, 2005.

[86] S. Zaefferer, S. I. Wright, and D. Raabe, “Three-dimensional orientation microscopy in a focused ion beam-scanning electron microscope: A new dimension of microstructure characterization,” *Metallurgical and Materials Transactions A: Physical Metallurgy and Materials Science*, vol. 39, no. 2. pp. 374–389, 2008.

BIOGRAPHICAL INFORMATION

Kranthi Balusu has been a doctoral student in Aerospace & Aeronautical engineering at the University of Texas at Arlington since Fall 2014. He has a master's degree in Applied Mechanics with specialization in biomedical engineering and a bachelor's degree in Aerospace engineering from the Indian Institute of Technology Madras, India. His research work has included widely different fields. His work in master's degree involved simulation of heat transfer in biological tissues. During his bachelors, he has worked on flame tomography. The common theme of his research being numerical solutions for engineering problems.

Kranthi aspires to work in the industry providing numerical solutions to engineering problems in emerging technologies. In this pursuit, he has worked for ANSYS as an intern involved in developing new Finite Element Method numerical routines for use in simulation of additive manufacturing. However, he intends to return to academia after service in the industry and nurture the future generation of engineers.